

Signal Processing for a Three-Component Transmitting  
(3CTx) Electromagnetic Device

by

Michael Finlayson

A thesis submitted in partial fulfillment  
of the requirements for the degree of  
Master of Science (MSc) in Geology

The Faculty of Graduate Studies  
Laurentian University  
Sudbury, Ontario, Canada

© Michael Finlayson, 2021

**THESIS DEFENCE COMMITTEE/COMITÉ DE SOUTENANCE DE THÈSE**  
**Laurentian University/Université Laurentienne**  
Faculty of Graduate Studies/Faculté des études supérieures

Title of Thesis Titre de la thèse	Signal Processing for a Three-Component Transmitting (3CTx) Electromagnetic Device		
Name of Candidate Nom du candidat	Finlayson, Michael William		
Degree Diplôme	Master of Science		
Department/Program Département/Programme	Geology	Date of Defence Date de la soutenance	April 23, 2021

**APPROVED/APPROUVÉ**

Thesis Examiners/Examineurs de thèse:

Dr. Richard Smith  
(Supervisor/Directeur(trice) de thèse)

Dr. Mostafa Naghizadeh  
(Committee member/Membre du comité)

Dr. Glenn McDowell  
(Committee member/Membre du comité)

Dr. Ian Ferguson  
(External Examiner/Examineur externe)

Approved for the Faculty of Graduate Studies  
Approuvé pour la Faculté des études supérieures  
Tammy Eger, PhD  
Vice-President, Research  
Vice-Rectrice à la recherche

**ACCESSIBILITY CLAUSE AND PERMISSION TO USE**

I, **Michael William Finlayson**, hereby grant to Laurentian University and/or its agents the non-exclusive license to archive and make accessible my thesis, dissertation, or project report in whole or in part in all forms of media, now or for the duration of my copyright ownership. I retain all other ownership rights to the copyright of the thesis, dissertation or project report. I also reserve the right to use in future works (such as articles or books) all or part of this thesis, dissertation, or project report. I further agree that permission for copying of this thesis in any manner, in whole or in part, for scholarly purposes may be granted by the professor or professors who supervised my thesis work or, in their absence, by the Head of the Department in which my thesis work was done. It is understood that any copying or publication or use of this thesis or parts thereof for financial gain shall not be allowed without my written permission. It is also understood that this copy is being made available in this form by the authority of the copyright owner solely for the purpose of private study and research and may not be copied or reproduced except as permitted by the copyright laws without written authority from the copyright owner.

## Abstract

When a three-component transmitter (3CTx) transmits simultaneously from all three transmitters, the signal measured in a receiver coil will be the sum of the three primary and secondary fields. In order to interpret the data, it is necessary to separate the signals from each transmitter. In a numerical experiment utilizing time-domain type sources, a synthesized signal comprised of the sum of three transmitter signals, a powerline signal and a low-frequency noise signal was created. Frequency spectra showed that for multiple specific combinations of base frequencies it is possible for the harmonics to be unique (not overlapping) and hence identifiable. For these combinations, the transmitter signals can be separated using a stacking filter in the time-domain. One specific combination is 30 Hz, 32.5 Hz, and 35 Hz for the three transmitters, when the powerline is operating at 60 Hz. The secondary fields generated by these three base frequencies were modelled using a wire-loop. Analyzing the response in three off-time and five on-time windows, it was determined that the maximum differences caused by having three different base frequencies are predictable and correctable. Thus, building and field testing the 3CTx is practical.

Key words:

Geophysics, electromagnetics, transmitter development, signal separation.

## Acknowledgments

I would like to thank my supervisor, Dr Richard Smith, for his guidance and support through my research. I would also like to thank NSERC for financial support through a Discovery Grant.

## Table of Contents

Thesis Defence Committee .....	ii
Abstract .....	iii
Acknowledgments .....	iv
Table of Contents .....	v
List of Tables .....	vi
List of Figures .....	vii
List of Appendices .....	x
Chapter 1 .....	1
Introduction .....	1
Chapter 2 .....	6
Theory .....	6
2.1 EM Induction .....	6
2.2 Wire-loop model .....	10
2.3 Fourier Transform (FT) and the Discrete Fourier Transform (DFT).....	15
2.4 Convolution.....	17
Chapter 3 .....	19
Waveform and Operating Base Frequencies.....	19
3.1 Base frequency Selection .....	20
3.2 Power Spectrum Analysis .....	22
3.3 Stacking Analysis.....	25
3.4 Conclusions for sets of base frequencies .....	31
Chapter 4 .....	33
Pulse shape and window selection .....	33
4.1 Secondary Field Estimation .....	33
4.2 Windowing.....	36
4.3 Conclusions for waveform configurations.....	49
Chapter 5 .....	50
Final Conclusions.....	50
Bibliography .....	52
Appendices.....	55

## List of Tables

Table 1: Summary of the base frequency selection analysis for the 3CTx device. .... 22

Table 2: Coefficient of Correlation for the linear regression performed in Figure 23. .... 46

## List of Figures

Figure 1: Current flowing through an arbitrary solid element (Modified from Grant & West, 1965). .....	6
Figure 2: Magnetic field $\mathbf{H}$ revolving around current density $\mathbf{J}$ (Modified from Grant & West, 1965). .....	8
Figure 3: Electrical field $\mathbf{E}(t)$ circulating around a time varying magnetic field (Modified from Grant & West, 1965). .....	8
Figure 4: Example of 2D EM induction, where one transmitter coil (Tx) and one receiver coil (Rx) are being used (Modified from Grant & West, 1965). .....	9
Figure 5: Grant and West (1965) wire-loop model. A current, $I_0$ flows around the transmitter, producing an electromagnetic force ( $\epsilon^P$ ) in the receiver coil and a current $I_1$ in the conductor. The subscript 0 refers to the transmitter loop, 1 refers to the conductor loop and 2 refers to the receiver loop. The superscripts $S$ and $P$ to the secondary and primary fields. The symbols $M_{ij}$ and $k_{ij}$ are the mutual inductances and coupling coefficients which represent the strength of the fields from coil $i$ to coil $j$ . (Figure taken from Grant and West, 1965.) .....	10
Figure 6: Shows the results of applying a Fourier transform of a periodic 10 Hz sine wave, with the upper panel only showing one cycle. The lower panel shows the results between $\pm 90$ Hz, beyond this all components have a value of zero. ....	17
Figure 7: 3CTx waveform for a 33.33 Hz signal. ....	19
Figure 8: Base waveforms for the three components of the 3CTx device, with the simulated local 60 Hz powerline waveform. ....	23
Figure 9: Full power spectrum for the waveforms found in Figure 8, with a sampling rate of $1.63 \times 10^{-5}$ s, indicating the spectrum is defined to very high frequencies. ....	24
Figure 10: Zoomed in version of the power spectrum from 0 Hz to 1000 Hz. Illustrating the differences between the signals analysed. Note the spectra contain only the odd harmonics for the source signals and the odd and even harmonics of the “dirty” powerline. ....	24
Figure 11: A 2000 ms combination of the 60 Hz powerline signal, the three source signals and a 0.5 Hz signal to simulate the movement of the device. ....	27
Figure 12: Zoomed in power spectrum for the mixed signal in Figure 11. Note only the odd harmonics for the source signals and all harmonics of the “dirty” powerline. ....	28
Figure 13: Results of applying a stacking analysis, dashed orange, compared to the original waveform, blue, A) 60 Hz powerline, B) 30 Hz signal, C) 32.5 Hz signal, D) 35 Hz signal. ....	29
Figure 14: Results of apply the stacking analysis for 4s, dashed orange, compared to the original waveform, blue, A) 60 Hz powerline, B) 30 Hz signal, C) 32.5 Hz signal, D) 35 Hz signal. ....	30

Figure 15: Estimation of the low frequency noise.....	31
Figure 16: Time-domain conductor secondary field responses for an isolated conductor utilizing the Grant and West wire-loop model (1965), for waveform configuration 1, where the pulse widths are fixed and the position of the windows relative to the pulse width is also fixed.....	35
Figure 17: All window locations for equal 6 ms pulse widths and fixed window positions, for the three base frequencies, where the on-time and off-time windows are identical. Note the labels at the top of the diagram refer to the respective window, for example W3 refers to Window 3.....	37
Figure 18: Windowed data results for the window locations from Figure 17 as a function of the $\tau$ value, A) Window 1, B) Window 2, C) Window 3. ....	38
Figure 19: Windowed data differences for the window locations from Figure 17 as a function of the $\tau$ value, A) Window 1, B) Window 2, C) Window 3.....	39
Figure 20: All window locations and pulse widths varied by the reduction factor, resulting in smaller window widths for larger base frequencies, A) 30 Hz signal, B) 32.5 Hz signal, C) 35 Hz signal. ....	41
Figure 21: Windowed data results for the window locations from Figure 20 compared to the $\tau$ value, A) Window 1, B) Window 2, C) Window 3. ....	42
Figure 22: Windowed data differences for the window locations from Figure 20 compared to the $\tau$ value, A) Window 1, B) Window 2, C) Window 3.....	43
Figure 23: Window differences by varying the base frequencies for the equal pulse width waveform for the off-time windows. ....	45
Figure 24: Plotting the differences for the differences between the frequencies. In addition, the difference between the estimated 32.5 Hz response and the 32.5 Hz response.....	48
Figure 25: Peak normalized window response as a function of $\tau$ , for the 30 Hz signal with a 6 ms pulse width A) off-time B) on-time .....	55
Figure 26: Peak normalized window response as a function of $\tau$ , for the 32.5 Hz signal with a 6 ms pulse width A) off-time B) on-time.....	56
Figure 27: Peak normalized window response as a function of $\tau$ , for the 35 Hz signal with a 6 ms pulse width A) off-time B) on-time .....	56
Figure 28: Peak normalized window response as a function of $\tau$ , for the 30 Hz signal with the pulse and window width unreduced A) off-time B) on-time .....	57
Figure 29: Peak normalized window response as a function of $\tau$ , for the 32.5 Hz signal with the pulse and window width reduced by a factor of 32.5/30 A) off-time B) on-time .....	58

Figure 30: Peak normalized window response as a function of  $\tau$ , for the 35 Hz signal with the pulse and window width reduced by a factor of 35/30 A) off-time B) on-time ..... 58

## List of Appendices

A	Windowed analysis for waveform configuration 1 .....	55
B	Windowed analysis for waveform configuration 2.....	57

## Chapter 1

### Introduction

The electromagnetic (EM) method is a widely used geophysical technique. Since the electrical resistivity of different earth materials ranges over many orders of magnitude, the EM methods are often capable of detecting a contrast between the material of interest and the background. In general, each EM survey measures the secondary response from the subsurface at a receiver.

The acquisition of EM data can be done in either the frequency-domain or the time-domain. In the frequency-domain method, the transmitter emits a current at a specific frequency. Both the in-phase and out-of-phase components will be measured at the receiver. As the system typically requires communication between the transmitter and receiver coil, these apparatuses tend to have a shallower depth of investigation (Burger et al., 2006). The time-domain approach on the other hand uses a source signal that undergoes more sudden transitions as a function of time and typically there is an active pulse time (on-time) and a time of zero current transmission (off-time). The system will most typically measure the secondary fields from the subsurface during the off-time (Burger et al., 2006), although some systems do measure the on-time data.

That time-domain EM signal can either be induced by a natural source (i.e. variations in the Earth's field due to lightning strikes or interactions with the field from the Sun) as observed in magnetotelluric surveys, or artificial sources (i.e. transmitters) as in most other EM surveys (Swift, 1988). In both cases, the process of induction is governed by Maxwell's equations (West & Macnae, 1991; Griffiths, 2013). In the case of time-domain artificial sources, a current is typically passed through a transmitter coil. This current has a specific waveform shape and period and the waveform at a base frequency, which is the inverse of the period. The current in the transmitter emits a primary magnetic field. Time variations in the current and primary field

will induce secondary currents in subsurface conductors. In turn, these secondary currents emit a secondary electromagnetic field that is measured in combination with the primary field at the receiver. After acquisition, it is common to apply filters, for example a stacking process to better improve the signal-to-ratio. A normal stacking filter refers to subtracting the negative half-cycle from the positive half-cycle and then averaging the resultant half cycles (Buselli & Cameron, 1996). As shown in Macnae et al. (1984) increasing the averaging (stacking) time improves the overall quality of the data acquired from a receiver.

In general, the EM method has a wide range of applications, ranging from the small scale (EM34 to look at shallow subsurface features) to the very large scale (using a magnetotelluric survey to map deep crustal structures). EM methods have also been successful in finding deposits containing Ni, Cu and platinum group elements (PGE) due to the high contrast between the host rocks and the very conductive massive sulfide ores (Swift, 1988; Watts 1997; Lymburner & Smith, 2015). A challenge in the exploration for new deposits is that the depths of these deposits can be greater than a kilometre (Watts, 1997). As the responses from these deep ore bodies are small and often below the background noise levels (Kolaj & Smith, 2014) they require a larger transmitter loop and lower base frequencies, to be detected in a conductive environment (Lymburner & Smith, 2015). Larger transmitter loops will require more powerful electronics to drive the current through the loop and more sophisticated electronics to turn off the current rapidly. The lower base frequencies inherently sacrifices high frequency information (Gisselø, 2018). An alternate approach is to construct a strong signal by summing together the fields from multiple three-component transmitters (3CTx).

The innovative 3CTx transmitter discussed in this thesis utilizes three orthogonal and co-located dipoles, with each component pointing in different directions, emitting a primary field that

excites the subsurface. The three corresponding secondary fields will be measured by receivers on the surface during a geophysical survey and multiple transmitter and receiver signals will be combined in an innovative manner, as described by Smith (2012). Data can be collected efficiently if the signals from the three transmitters that can be clearly distinguished from each other (Smith, 2018).

A 3CTx can be used in both ground and airborne applications. Smith (2012) argues that the three components can be combined so as to generate a primary magnetic field in any direction in the subsurface, ensuring that the three-component transmitter will never be null coupled with a target, no matter the orientation of the target or the position of the transmitter or target. In a conventional single transmitter loop ground survey, it may take several attempts to find a transmitter position that couples adequately with the subsurface conductor (Kolaj & Smith, 2014), which can be a time-consuming process. Furthermore, Smith (2012), suggests a procedure for combining the primary fields from many transmitter positions of the three-component transmitter so as to increase the signal-to-noise ratio of the target. A similar procedure has been applied to single-component transmitter data by Lymburner and Smith (2015) and Kolaj and Smith (2015). These arguments apply for configurations where the transmitter and receiver can be on the ground, but Smith (2012) points out that the transmitters could be in the air and the receivers on the ground, or vice versa. It might also be possible to have both in the air, for example, using a large aircraft for the transmitter and drones for the receivers.

There is also an airborne configuration comprising at least one three-component transmitter and at least one three component receiver. In this case, the multiple-component transmitter and receiver data can be combined geometrically to cancel out the primary field and leave only the in-phase secondary field (Smith, 2018). As highly conductive bodies, such as nickel, are

dominated by an in-phase secondary response, this system would be capable of detecting this type of body.

The 3CTx has a number of potential advantages. Firstly, the data from the three transmitters can be combined to increase the signal-to-noise ratio of a small target at great depth that has a small response (Smith, 2012). When this is combined with data from multiple transmitter positions (Kolaj and Smith, 2014), it is possible to gain further improvements. Secondly, a 3CTx can identify extremely conductive bodies (Smith, 2018) using the nine independent responses. It can also identify the small response of poorer conductors in the area. Thirdly, the multiple components provide information to determine the strike and dip of plate-like conductors (Desmarais & Smith, 2016). Some of these advantages require comparing the responses from different transmitters in time gates or windows, so the data should be comparable.

Digital EM receivers normally sample the response using a very large number of equi-spaced discrete samples during and after, when the transmitter current is on. By binning and averaging the samples that are in a specific set of time intervals (or windows), it is possible to increase the signal-to-noise ratio (Becker & Cheng, 1987; Nabighian & Macnae, 1991). The widths of these windows frequently increase with time, as transients with rapid decays at early time require narrower windows close to the pulse. Late time samples require a wider window due to the response of the secondary signal being small compared with the noise and a wider window will remove some of this noise (Macnae et al., 1984; Nabighian & Macnae, 1991).

The intention of this project is to outline the necessary background information that will allow for the building of a prototype, laboratory testing, and initial testing of a 3CTx. Due to the COVID-19 pandemic this aspect of the project has not been able to be carried out. As a result, the purpose of this thesis is to determine appropriate base frequencies that the 3CTx can transmit

simultaneously in such a way that the signals from one transmitter do not interfere with those from the other two (Desmarais & Smith, 2016; Smith, 2018). This was determined using trial and error testing in an Excel spreadsheet that used conditional formatting to ensure the harmonics did not coincide and hence interfere. Next, spectral analysis was used to determine if there was any overlap between the three coil frequencies of the 3CTx. A method was then devised to separate the signals using a stacking filter in the time-domain, for one of the cases when the spectral analysis showed there was no overlap between the signals. We then investigated the impact on the secondary field of using these different base frequencies for each component of the 3CTx. This was done assuming a wire-loop model. We then experimented with modifying the window locations and waveform to minimize the differences between similar windows when using different base frequencies. As the frequency changes, we desire small differences so the data from the different transmitters can be compared. We found that the variation of the windowed secondary field response with frequency was approximately linear. This suggests that a linear combination of different frequencies could give even smaller differences.

## Chapter 2

### Theory

#### 2.1 EM Induction

Electromagnetic fields are governed by Maxwell's equations, such as Ampere's and Faraday's laws. The electromagnetic fields can be related to each other by empirical constitutive laws such as Ohm's law, which states that the voltage difference ( $\Delta V$ ) is proportional to the current ( $I$ ) passing through an element, shown in Figure 1, with the constant of proportionality being the resistance ( $R$ ).

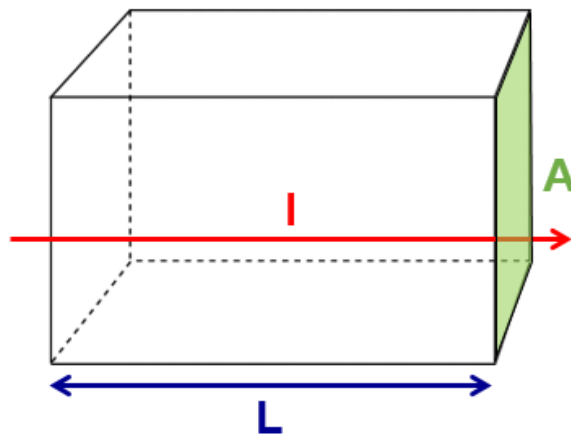


Figure 1: Current flowing through an arbitrary solid element (Modified from Grant & West, 1965).

Mathematically this empirical law is:

$$R = \frac{-\Delta V}{I}. \quad (1)$$

For a solid material, the resistance is proportional to the length ( $L$ ), in blue, and inversely proportional to the cross-sectional area ( $A$ ), in green. Dividing the resistance by the length and multiplying by the area gives a quantity, called the resistivity ( $\rho$ ) that is independent of the

length and area. As the electric field is the voltage difference per unit length and the current density is the current per unit area, Ohm's law can be written as

$$\mathbf{E} = \rho \mathbf{J}, \quad (2)$$

where,

$$\rho = R \frac{A}{L}. \quad (3)$$

Ohm's law can break down in subsurface conditions when current densities are high ( $> 1 \text{ A/m}^2$ ), but it is normally a good simplifying assumption in electromagnetic surveys (Grant & West, 1965).

Ampere's law states that the current density ( $\mathbf{J}$ ), which is flowing as a result of Ohm's law, produces a magnetic field intensity ( $\mathbf{H}$ ), which is a vector quantity. Using the right-hand rule, we can determine the direction of the magnetic field, by pointing our thumb in the direction of the current and curling the fingers towards the palm, with the fingers pointing in the direction of the magnetic field intensity. The magnetic field is hence said to curl around the current density. A graphical representation of the curling field is shown below in Figure 2. In the figure, a displacement current  $d\mathbf{D}/dt$  is added to the current density, but this is typically ignored at the frequencies at which inductive electromagnetic prospecting systems operate.

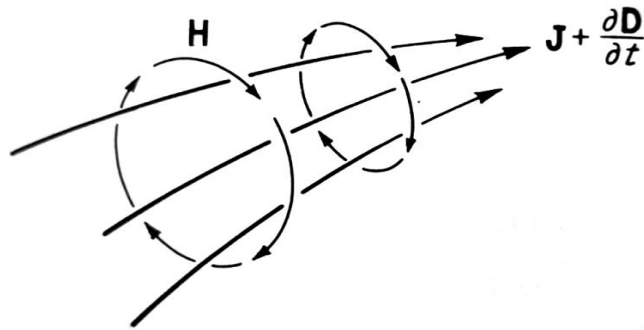


Figure 2: Magnetic field  $\mathbf{H}$  revolving around current density  $\mathbf{J}$   
(Modified from Grant & West, 1965).

Faraday's law states that there is an electric field circulating about any time-varying magnetic field. The magnitude of the electric field is proportional to the negative rate of change of the magnetic flux ( $-d\mathbf{B}/dt$ ). This is depicted graphically in Figure 3. If the electric field exist in a material that has a non-zero conductivity ( $\sigma$ ), then the electric field results in a flow of current,  $\mathbf{J}$ , given by a rewritten form of Ohm's law  $\mathbf{J} = \sigma\mathbf{E}$ , where comparison with Equation (2) shows that the conductivity  $\sigma = 1/\rho$ .

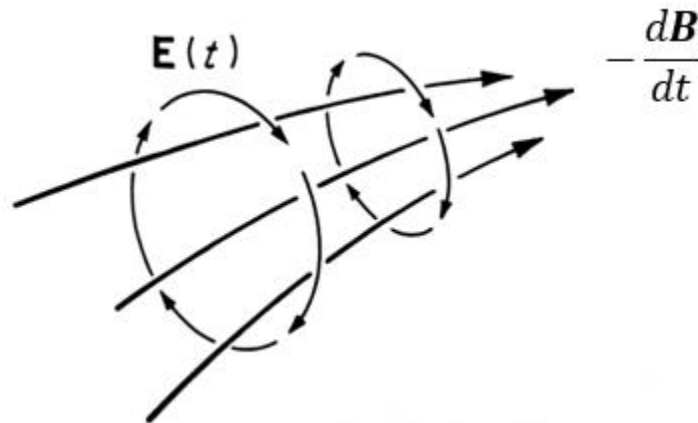


Figure 3: Electrical field  $\mathbf{E}(t)$  circulating around a time varying magnetic field  
(Modified from Grant & West, 1965).

These laws help us understand how electromagnetic prospecting systems operate, a schematic diagram of which can be found in Figure 4. First, current is driven to circulate in the transmitter coil (Tx), it generates a primary magnetic field, green lines, following Ampere's law. This magnetic field radiates to the receiver coil (Rx), and through the subsurface. If the current is driven so as to vary as a function of time, then so does the primary field in the subsurface. This time-varying field creates a circulating electrical field, represented by the brown circles, following Faraday's law. When these electrical fields exist in a conductive body in the subsurface, they produce a current density flux through the conductor following Ohm's law. The current through the conductive induces another magnetic field, called the secondary field, shown with red lines. This field exists at the surface and is also measured by the receiver coil (Rx) (Grant & West, 1965; West & Macnae, 1991).

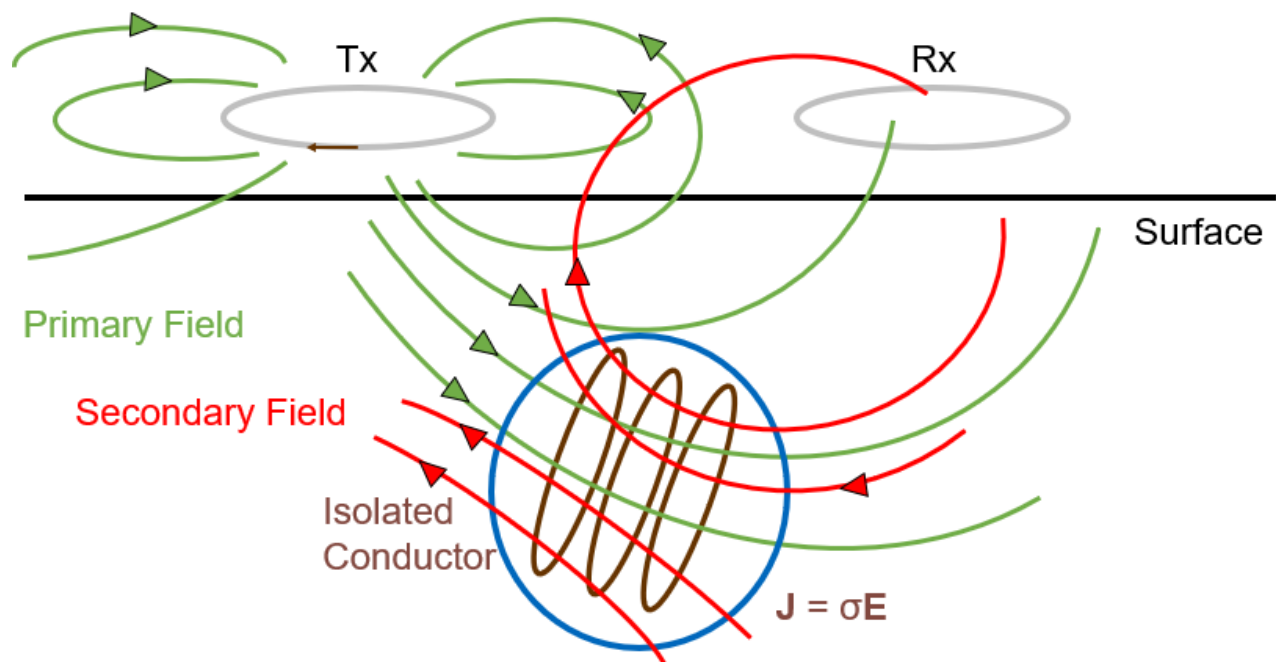


Figure 4: Example of 2D EM induction, where one transmitter coil (Tx) and one receiver coil (Rx) are being used (Modified from Grant & West, 1965).

The above diagram is for a one-component transmitter, however, in the event a 3CTx device is used, each transmitter component will have their own primary field and associated secondary fields. Hence, there will be three secondary fields at each receiver coil used in a given survey. As each field is a three-component vector, there will be nine secondary-field components in all, when a 3CTx is used in combination with a three-component receiver.

## 2.2 Wire-loop model

The wire-loop model is a simple representation of the subsurface conductor as a single loop, with self-inductance,  $L$ , and resistance,  $R$ . Additionally, this model represents the transmitter and receiver as dipoles, as shown below in Figure 5.

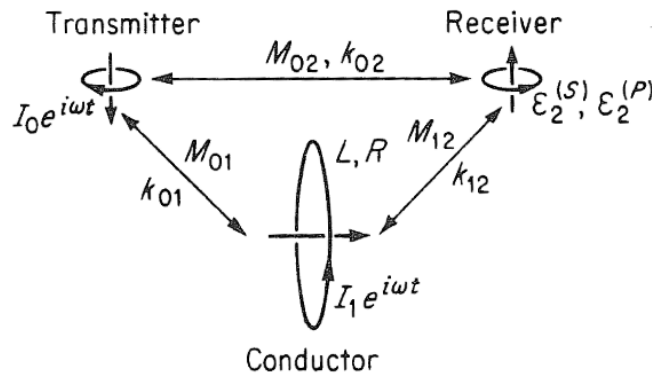


Figure 5: Grant and West (1965) wire-loop model. A current,  $I_0$  flows around the transmitter, producing an electromagnetic force ( $\epsilon^P$ ) in the receiver coil and a current  $I_1$  in the conductor. The subscript 0 refers to the transmitter loop, 1 refers to the conductor loop and 2 refers to the receiver loop. The superscripts  $S$  and  $P$  refers to the secondary and primary fields. The symbols  $M_{ij}$  and  $k_{ij}$  are the mutual inductances and coupling coefficients which represent the strength of the fields from coil  $i$  to coil  $j$ . (Figure taken from Grant and West, 1965.)

The following derivation summarizes the process to calculate the response function for the single-loop conductor model developed by Grant and West (1965).

The alternating current  $I_0 e^{i\omega t}$  flowing around the transmitter coil has an alternating magnetic field. According to Faraday's law, it creates a voltage or electromotive force (emf),  $\epsilon$  around the

subsurface conductor loop and the receiver on the surface. The mathematical expression of Faraday's law relates the current in a loop  $I_i$  to the voltage in a loop  $\varepsilon_j$ , through:

$$\varepsilon_j = -M_{ij} \frac{dI_i}{dt}, \quad (4)$$

where,  $M_{ij}$  is the mutual inductance,  $i$  refers to the subscript of the loop carrying the current, and  $j$  refers to the loop the voltage is created in. As previously stated in Figure 5, the subscript 0 refers to the transmitter loop, 1 refers to the conductor loop and 2 refers to the receiver loop. Looking at an example,  $M_{01}$  refers to mutual inductance that relates the transmitter coil to the conductor.

Similarly, alternating current in the transmitter loop also produces voltage in the receiver loop,  $\varepsilon_2^P$ , as defined below:

$$\varepsilon_2^P = -M_{02} \frac{d}{dt} I_0 e^{i\omega t} = -i\omega M_{02} I_0 e^{i\omega t}, \quad (5)$$

where, we have now included a harmonic time dependence in the current flowing in the transmitter,  $i$  is the complex number  $\sqrt{-1}$ ,  $\omega$  is the angular frequency of the harmonic time dependence, in radians/second, and  $M_{02}$  is the mutual inductance between the transmitter and receiver.

With this time dependence, the emf induced through the underground circuit is

$$\varepsilon_1 = -i\omega M_{01} I_0 e^{i\omega t}. \quad (6)$$

Defining an emf in the underground circuit,  $\varepsilon_1^\dagger$ , that is the sum of the voltage drop across the resistance of the circuit and the back emf generated by the self-inductance when a current  $I_1 e^{i\omega t}$  flows around the subsurface loop. Thus,

$$\begin{aligned}\varepsilon_1^\dagger &= -RI_1 e^{i\omega t} - L \frac{d}{dt} I_1 e^{i\omega t}, \\ \varepsilon_1^\dagger &= -(R + i\omega L)I_1 e^{i\omega t}.\end{aligned}\tag{7}$$

In order to find the current  $I_1$ , the total emf must vanish as the model is a closed circuit, i.e.,

$$\varepsilon_1 + \varepsilon_1^\dagger = 0\tag{8}$$

Substituting Equation (6) and (7) into (8) and rearranging for  $I_1 e^{i\omega t}$ , we get

$$\begin{aligned}I_1 e^{i\omega t} &= \frac{-i\omega M_{01}}{R_1 + i\omega L_1} I_0 e^{i\omega t}, \\ I_1 e^{i\omega t} &= -\frac{M_{01}}{L_1} \frac{i\omega L_1 (R_1 - i\omega L_1)}{R_1^2 + \omega^2 L_1^2} I_0 e^{i\omega t}.\end{aligned}\tag{9}$$

The secondary magnetic field at the receiver coil, which this current produces, is

$$\varepsilon_2^S = -i\omega M_{12} I_1 e^{i\omega t},\tag{10}$$

where  $M_{12}$  is the mutual inductance between the underground circuit and the receiver loop.

Normalizing the secondary emf in the receiver by the primary gives

$$\frac{\varepsilon_2^S}{\varepsilon_2^P} = \frac{-i\omega M_{12} I_1 e^{i\omega t}}{-i\omega M_{02} I_0 e^{i\omega t}},$$

$$\frac{\varepsilon_2^S}{\varepsilon_2^P} = -\frac{M_{01}M_{12}}{M_{02}L_1} \left[ \frac{i\left(\frac{\omega L_1}{R_1}\right)\left(1 - \frac{i\omega L_1}{R_1}\right)}{1 + \left(\frac{\omega L_1}{R_1}\right)^2} \right]. \quad (11)$$

Substituting the response parameter  $\tau = \omega L_1/R_1$ , the Equation (11) simplifies to

$$\frac{\varepsilon_2^S}{\varepsilon_2^P} = -\frac{M_{01}M_{12}}{M_{02}L_1} \left[ \frac{\tau^2 + i\tau}{1 + \tau^2} \right]. \quad (12)$$

Equation (12) can also be rewritten in terms of the coupling coefficient,  $k_{ij} = M_{ij}/\sqrt{L_i L_j}$ ,

$$\frac{\varepsilon_2^S}{\varepsilon_2^P} = -\frac{k_{01}k_{12}}{k_{02}} \left[ \frac{\tau^2 + i\tau}{1 + \tau^2} \right], \quad (13)$$

where, the subscript 0 refers to the transmitter loop, 1 refers to the conductor loop and 2 refers to the receiver loop. The coupling coefficients change as a result of the circuit position and orientation and not the subsurface electric properties (Grant & West, 1965). Thus, when using the wire-loop model, the coupling coefficients have minimal bearing on the frequency or temporal response, they are primarily used to determine how the response along a profile varies as the relative position of the circuits change.

The “response function”, represented by the expression contained within the square brackets, is dependent on both the electrical properties of the ground and the frequency. The two limiting cases of the wire-loop model response are the resistive limit and the inductive limit.

The resistive limit occurs when  $\tau$  is small (Grant & West, 1965; Smiarowski, 2012), giving

$$\frac{\varepsilon_2^S}{\varepsilon_2^P} = -\frac{k_{01}k_{12}}{k_{02}} \left[ \frac{i\omega L_1}{R_1} \right]. \quad (14)$$

As can be seen, at these small values of  $\tau$ , the response is proportional to  $L/R$  and  $i\omega$ . Anything proportional to  $i\omega$  in the frequency-domain is proportional to the derivative in the time-domain.

As the resistance of the subsurface conductor increases there is a decrease in the response.

The inductive limit occurs at very large values of  $\tau$ , or when the frequency and or the self inductance is large or the resistance is approximately zero. In this case the value of the response function is equal to 1, implying that the secondary field is a scaled version of the primary field (Grant & West, 1965; Smiarowski, 2012). Mathematically, this can be written as

$$\frac{\varepsilon_2^S}{\varepsilon_2^P} = -\frac{k_{01}k_{12}}{k_{02}}. \quad (15)$$

Hodges & Chen (2015) used the wire-loop model to analyze the geo-bandwidth of a subsurface conductor. They define geo-bandwidth as the EM response across the shortest to longest time constant for all channels used. Using the idea of the geo-bandwidth, it was determined that the wire-loop model is good for analyzing the response amplitudes of weak and strong conductors (Becker & Cheng, 1987).

As the wire-loop model is an effective way to analyze subsurface conductive features it can be used in a variety of ways. First, a plate-like structure can be represented by a wire-loop that is 70% of the size of the plate and has an appropriately selected response parameter,  $\tau$ , selected to model the data at specific delay time -- primarily late delay times (McNeill et al., 1984; Smiarowski, 2012). Secondly, a spherical subsurface conductor can be represented as a wire-loop by placing the plane of the loop perpendicular to the transmitter primary field, as illustrated in Figure 4. As the transmitter position changes, the orientation of the primary will change and the wire-loop orientation will also change to be perpendicular to the primary. To that end, it was

determined that the wire-loop model was an appropriate model to use when designing the transmitter pulse and window positions for the 3CTx device.

The wire-loop model is used to represent how the subsurface conductor loop is geometrically coupled to the transmitter and receiver surface geometry. It can also be used to forward model the secondary response of a system, if the resistance, inductance and waveform characteristics of the transmitter are specified. The model will be used later in Chapter 4, as we vary the waveform and the subsurface conductor parameter,  $\tau$ , assuming a constant coupling coefficient.

### 2.3 Fourier Transform (FT) and the Discrete Fourier Transform (DFT)

A function  $f(t)$  and its complex Fourier transform are related by the Fourier transform relationships (Shatkay, 1995; Bracewell, 2000).

$$f(t) = \frac{1}{2\pi} \int_{-\infty}^{\infty} F(\omega) e^{i\omega t} d\omega, \quad (16)$$

$$F(\omega) = \int_{-\infty}^{\infty} f(t) e^{-i\omega t} dt. \quad (17)$$

Equation (16) describes the inverse FT process and Equation (17) is the Fourier transform process, which provides a means for finding the amplitudes at each frequency,  $\omega$  (Shatkay, 1995). The FT process converts a time-domain signal into the Fourier (or frequency) domain. This is sometimes useful as the signals are simpler to understand or manipulate in the frequency-domain.

While Equation (16) and (17) describe the FT for a continuous signal of infinite length and can be defined at an infinite number of frequencies. In practise, signals are sampled at regular intervals and comprise a finite number of samples (Shatkay, 1995). Ensuring that the signal is

adequately sampled and not aliased, it is necessary to sample the signal up to and including the Nyquist frequency,  $\omega_s$ , which is at least twice the highest frequency present in the original signal,  $\omega_N$ , or mathematically

$$\omega_s \geq 2\omega_N. \quad (18)$$

The discrete Fourier transform (DFT) is an analogous transform for discretely sampled signals of finite length. This transform maps discrete periodic sequence  $f(k)$  (where  $k$  is an integer representing equi-spaced samples, and the period is  $N$ ) to another sequence  $F(j)$  of complex frequency coefficients. Equation (19), and Equation (20) are relations between the discrete periodic function and its discrete Fourier transform (Oliphant, 2006). The DFT is defined as,

$$F(j) = \Delta t \sum_{k=0}^{N-1} f(k) e^{\frac{-2\pi i k j}{N}}, \quad (19)$$

where,  $0 \leq j \leq N-1$ ,  $i$  is the imaginary number,  $N$  is the number of samples,  $\Delta t$  is the sampling interval, and  $f(k)$  is the discrete value of the sequence in the time-domain at sample  $k$ . While, the inverse DFT is defined as,

$$f(k) = \frac{1}{N\Delta t} \sum_{j=0}^{N-1} F(j) e^{\frac{2\pi i k j}{N}}, \quad (20)$$

where,  $0 \leq k \leq N-1$ , and  $F(j)$  are the frequency-domain coefficients.

The fast Fourier transform (FFT) is a way of calculating the DFT quickly and efficiently. Using a butterfly algorithm, the FFT requires that the period to be a power of two, i.e.,  $N = 2^m$  (Oliphant, 2006). The  $\Delta t$  associated with Equation (19) and Equation (20) allow for the correct time units to be preserved.

An example of the FFT applied to a 10 Hz sine wave is seen in Figure 6, where  $f(k)$  is shown in the top panel and the frequency transform,  $F(j)$ , in the bottom panel has two non-zero signals at the frequency of the sine wave that are purely imaginary.

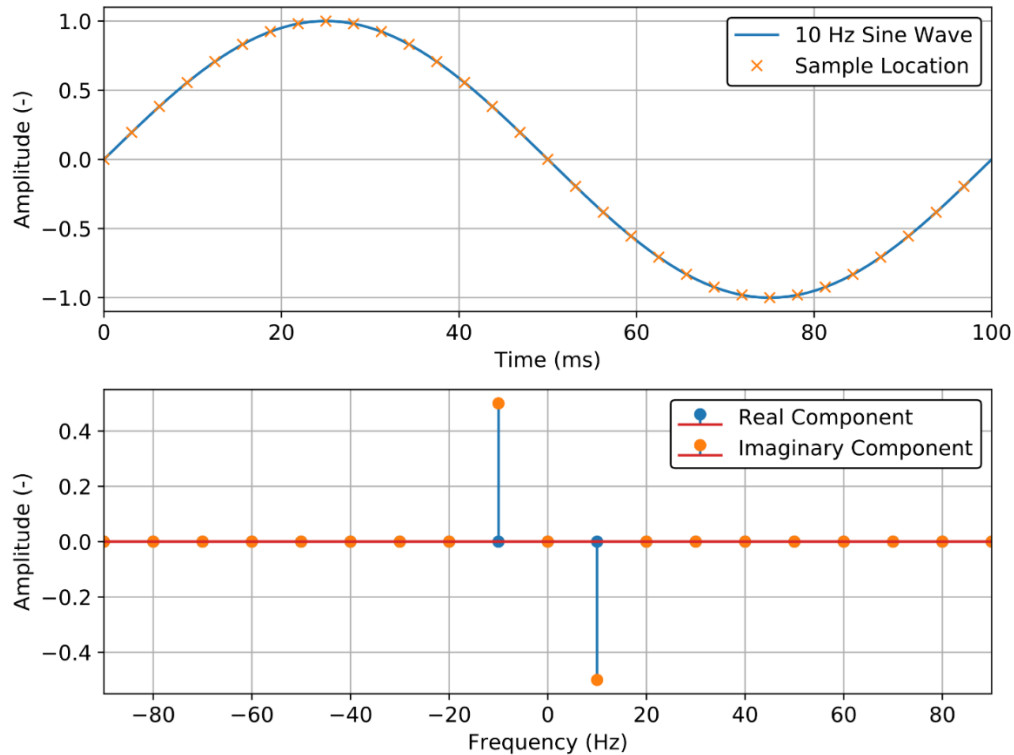


Figure 6: Shows the results of applying a Fourier transform of a periodic 10 Hz sine wave, with the upper panel only showing one cycle. The lower panel shows the results between  $\pm 90$  Hz, beyond this all components have a value of zero.

All Fourier transforms described in the thesis involved an integral number of transmitter cycles, to avoid discontinuities and the introduction of serious frequencies.

## 2.4 Convolution

Convolution is a signal processing operation that takes two signals and produces a third (Strauss, 2000). Convolution is necessary in order to estimate the response of the system to other non-impulsive signals. For example, the Fourier transform of the 3CTx signals need to be multiplied

with frequency response on the right side of Equation (13) to get the emf associated with the underground circuit.

Convolution can be completed either in the time or frequency-domain. Equation (21),

$$s(t) = f(t) * g(t) = \int_{-\infty}^{\infty} f(t - \alpha)g(\alpha) d\alpha, \quad (21)$$

is the mathematical formula for convolution in the time-domain, representing an integral of the product of the two input functions after one has been reversed and shifted by the integration variable. The integral is evaluated for all values of  $t$ .

The alternative approach is to complete the convolution in the frequency-domain using Equation (22),

$$s(\omega) = f(\omega)g(\omega), \quad (22)$$

where the convolution is a simple multiplication. The latter process requires taking the FT of both signals, multiplying them together, and then applying an inverse FT to bring the result back to the time-domain. Generally, the time-domain integral is considered more complex and can have slower computations times. The frequency-domain approach of using Equation (22), is generally more efficient, especially when the array has a length of  $2^m$  and the FFT can be used (Oliphant, 2006).

## Chapter 3

### Waveform and Operating Base Frequencies

As a receiver coil measures the sum of the three secondary fields, it is necessary to separate the responses created by each source signal. First, a decision matrix was used to identify a suitable base frequency set for the 3CTx device. To that end, we began by constructing a synthetic signal comprised of the sum of three transmitter signals, a powerline signal and a low-frequency noise that simulates the movement of the device. A spectral analysis in the frequency-domain will be used to check if there is separation of the harmonics. Then, the synthetic data were stacked to demonstrate that the source signals could be separated.

Each transmitter coil is assumed to carry a current with a bi-directional waveform that repeats periodically. For the purpose of this exercise, the 3CTx device will utilize a total pulse width of 6 ms, with a 4.5 ms exponential ramp on and a 1.5 ms linear ramp off. An example of the device waveform at a base frequency of 33.33 Hz is shown in Figure 7.

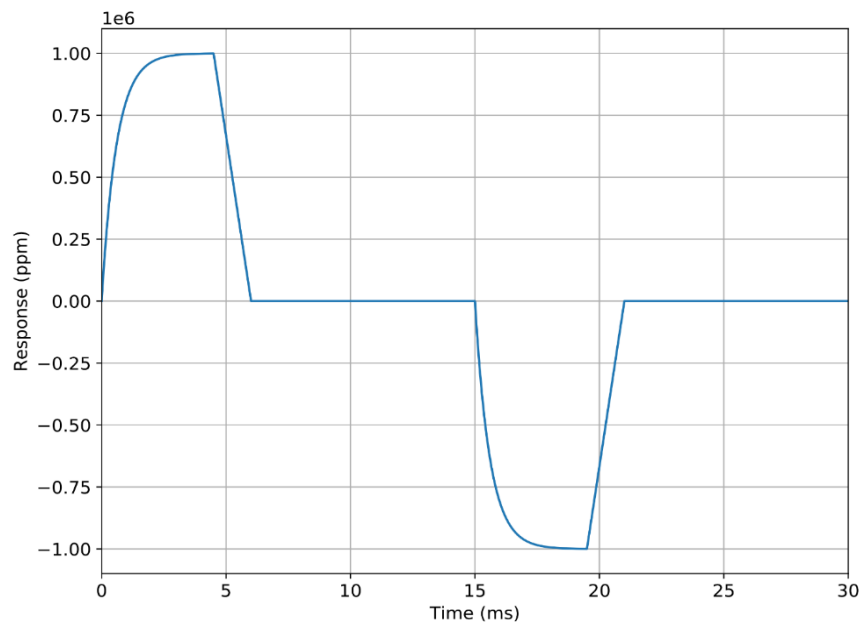


Figure 7: 3CTx waveform for a 33.33 Hz signal.

This pulse shape was selected as it is similar to the EM-37 pulse, which has a good signal-to-noise ratio (McNeill et al., 1984).

### 3.1 Base frequency Selection

As it is not possible to separate signals from different transmitters that have the same base frequency (Desmarais & Smith, 2016), we need a system with different base frequencies that can be clearly distinguished from each other (Smith, 2018).

The waveforms for each transmitter have a second half that is the negative of the first half, so they only have the odd harmonics, where:

$$\text{Odd harmonic} = 3f, 5f, 7f, 9f, 11f, 13f, 15f, \dots, \quad (23)$$

where,  $f$  is a base frequency. If we want the waveforms to be separable, none of the odd harmonics for all three transmitters should coincide. The powerline signal generally has odd harmonics, but in some cases, it can have even harmonics, where:

$$\text{Even harmonic} = 2f, 4f, 6f, 8f, 10f, 12f, 14f \dots \quad (24)$$

The odd harmonics of the three transmitters should not coincide with any of the odd or even harmonics of the powerline frequency (Smith, 2018). Similarly, the low-frequency noise should be below the lowest harmonic of each transmitter. When any of these conditions are not met, the signal from one transmitter component will mix and the individual signals cannot be separated (Desmarais & Smith, 2016). It is also desirable to have the harmonics offset as far as possible from each other to reduce the stacking time required to get good signal-to-noise ratios. In general, lower base frequencies are more useful for detecting slow decays but require longer stacking times to collect useful data.

Using an iterative trial-and-error process we experimented with a number of set combinations. In Excel, we began by calculating the first 200 harmonics for each base frequency in the set. We then compared them against each other and all the harmonics of the 60 Hz powerline using conditional formatting to find if that harmonic was found in any other list of harmonics. In a field experiment, if mixing is suspected, then this Excel sheet could be used to determine another appropriate set of frequencies. Such a situation might arise at a site where there is a non 60 Hz powerline frequency. As there is an infinite number of combinations, the best approach is to use some commonly-used frequencies to help narrow down the search.

As a result we have selected three suitable possibilities: Set 1 containing 15, 22.5 and 30 Hz; set 2 with 30, 32.5 and 35 Hz; and set 3 with 79, 97 and 113 Hz. Set 1 and set 2 contain odd harmonics further from the powerline frequencies, while set 3 would be useful in areas where more rapid decays are of interest and longer stacking can be used to separate harmonics close to each other.

Set 1 contains base frequencies that are below or close to 20 Hz, so are useful for very slow decays, and deep exploration associated with the signals that can be measured at late time. However, low frequencies can mean less stacks, which will result in increased noise levels, especially for an airborne system (Konieczny et al., 2016), which cannot stop to acquire more stacks. Hence airborne systems require particular care if such low frequencies are used to ensure low noise levels. Otherwise, the high noise levels will swamp the signal at late time and negate the potential increased depth of exploration. Set 2 has a moderate depth of exploration and avoids the sub 20 Hz base frequency. Further, the frequencies are quite similar, meaning that the length of the off-time responses are similar in length. Making it easier to determine the window positions found in Chapter 4. Set three was designed for short acquisition times and shallow

depth of exploration, due to the higher base frequencies. These higher base frequencies would limit the depth of penetration in areas where there is thick conductive cover (Konieczny et al., 2016). A summary of the discussion of these three sets is shown below in Table 1.

Table 1: Summary of the base frequency selection analysis for the 3CTx device.

Criteria	15 Hz, 22.5 Hz, 30 Hz	30 Hz, 32.5 Hz, 35 Hz	79 Hz, 97 Hz, 113 Hz
<b>No overlapping odd harmonics</b>	Yes	Yes	Yes
<b>Offset of odd harmonics from each other and powerline harmonics</b>	2.5 Hz	2.5 Hz	1 Hz
<b>Practicality of deployment</b>	Greater depth of exploration but increased noise, particularly for airborne system.	Moderate depth of exploration; similar off-time range makes comparison of response at each frequency easier.	Shallow depth of exploration; short acquisition time.

We have selected set 2, containing 30, 32.5 and 35 Hz to demonstrate that the harmonics do not overlap and that it is possible to separate the source signals, low frequency noise (estimated using a 0.5 Hz sinusoidal wave) and a noisy 60 Hz powerline signal.

### 3.2 Power Spectrum Analysis

A DFT was used to calculate the power spectrum,  $PS(\omega)$  of set 2 by combining the real and imaginary parts of the Fourier transform,  $F$ ,

$$PS(\omega) = \Re^2 + \Im^2, \quad (25)$$

where,  $\Re$  is the real component of  $F$ , and  $\Im$  is the imaginary component of  $F$ .

The 3CTx source signals were constructed with a 6 ms pulse width for all three frequencies. A modified square wave was used to approximate the behaviour of a “dirty” local powerline, with high frequencies. This was achieved by making the powerline signal more like a square wave (Macnae, 2017). The dirty aspect was achieved by adding a small pulse to the first part of the waveform, but not the second; this adds even harmonics to the signal. The wavelets used for the analysis are shown in Figure 8, with the associated power spectrum is in Figure 9 and a zoomed in power spectrum illustrating the differences between the base frequencies, in Figure 10.

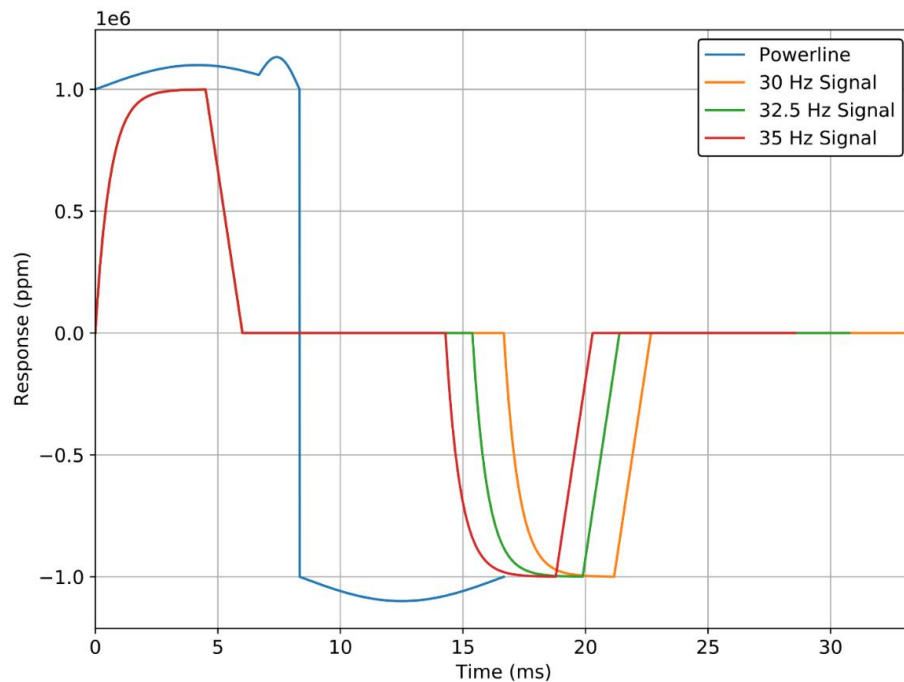


Figure 8: Base waveforms for the three components of the 3CTx device, with the simulated local 60 Hz powerline waveform.

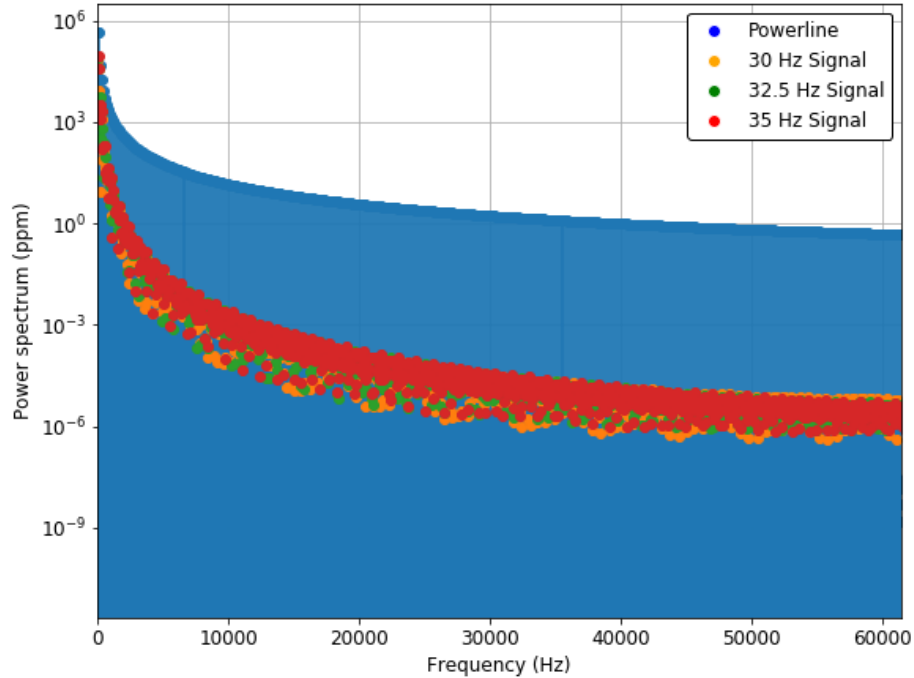


Figure 9: Full power spectrum for the waveforms found in Figure 8, with a sampling rate of  $1.63 \times 10^{-5}$  s, indicating the spectrum is defined to very high frequencies.

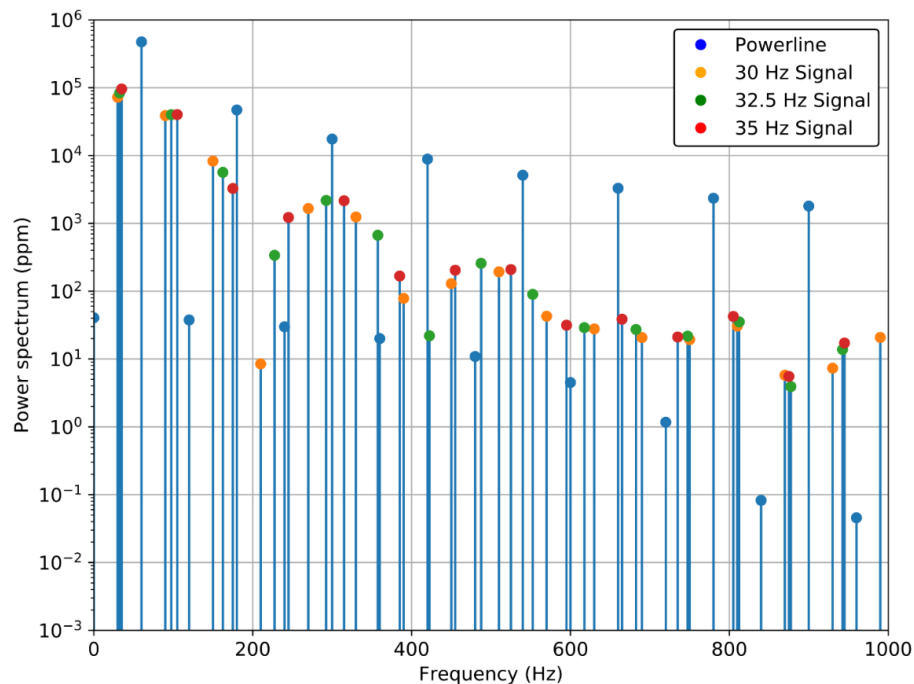


Figure 10: Zoomed in version of the power spectrum from 0 Hz to 1000 Hz. Illustrating the differences between the signals analysed. Note the spectra contain only the odd harmonics for the source signals and the odd and even harmonics of the “dirty” powerline.

The odd harmonics, picked utilizing the `numpy.fft` library, of the powerline are at 180, 300, 420 Hz,..., while the even harmonics are at 120, 240, 360, 480 Hz,... The odd harmonics of 30 Hz are at 90, 150, 210, 270, 330, 390, 450 Hz,.... These two sets of harmonics will never coincide, as the powerline harmonics are always even powers of ten and the odd harmonics of 30 Hz are odd powers of ten. The odd harmonics of 32.5 Hz are 97.5, 162.5, 227.5, 292.5, 357.5, 422.5, 487.5 Hz,... and the odd harmonics of 35 Hz are 105, 175, 245, 315, 385, 455 Hz, ... The 35 Hz series always ends in 5 Hz and the 32.5 series end in 2.5 or 7.5 Hz, so these two series will not coincide with each other or either of the previous series. The closest they will come to each other is 2.5 Hz. This can be illustrated on Figure 10 which shows all the harmonics between the 0 Hz and 1000 Hz. There are a number of locations where the harmonics appear close, for example at 357.5 and 360 Hz and 420 and 422.5 Hz, but in each case, they are offset by 2.5 Hz. This illustrates that this combination of the three base frequencies is a valid selection for the 3CTx. Similar arguments apply for the other sets of base frequencies.

### 3.3 Stacking Analysis

The final test for verifying the suitability of chosen sets is to use a stacking filter applied to synthetic data made from summation of the three transmitter signals, a powerline signal and a low-frequency noise signal. Stacking is basically a moving average linear filtering process (Kingman et al., 2004). In the processing of geophysical data, it averages a periodic waveform to reduce noise at all but the desired set of frequencies so as to estimate the periodic signal and to better improve the signal-to-noise ratio (Mcfadden & Kravis, 1986; Kingman et al., 2004; Rudd et al., 2017). For example, a stacking process can be used to reduce the coherent noise generated by powerlines and low frequency noise generated by movement of the device (Macnae et al., 1984; Lee et al., 2001).

Waveforms are often bipolar, with a positive half-cycle being followed by a negative half-cycle (e.g., Figure 8). This allows constant noise to be removed using a normal stacking filter that subtracts the negative half-cycle from the positive half-cycle (Buselli & Cameron, 1996). This doubles the half-cycles and removes any constant level. However, this stacking process is not capable of removing linear drift from a data set and such drift will result in an additional offset in the stacked result. More generally, for a slowly varying signal, this stacking process will result in visible errors (Kingman et al., 2004).

The approach we took to overcome the disadvantages of the normal stacking was by applying the Halverson stacking filter first. This filter was developed in the 1960s to remove linear drift in data; and was also found to substantially reduce low-frequency noise. The filter is a weighted combination of a half-cycle with the previous and subsequent half-cycles. Halverson determined that the best weights for his filter were  $-\frac{1}{4}$ ,  $\frac{1}{2}$ ,  $-\frac{1}{4}$  (Kingman et al., 2004). Mathematically, the filter is written as,

$$HF = \frac{-1}{4}f(x) + \frac{1}{2}f(x+h) - \frac{1}{4}f(x+2h), \quad (26)$$

where,  $HF$  is the array produced by the Halverson stacking filter,  $N$  is the number of points in array  $f$ ,  $x$  is an iteration operator  $x = 0, 1, 2, 3, \dots, N - 2h, N - h$ , and  $h$  is the number of points in one half-cycle of the base frequency of interest. Specifically, this is an element-wise moving-average filter. It starts at the first element of the second half-period, multiplying that by 0.5. It then takes the first element of the half-period both before and after and multiplies each by -0.25. The value is then summed. The process is then iterated for all elements in the waveform. In this way, the entire signal can be reduced down to a single waveform. After, the negative half-period

is subtracted from the positive half-period and halved. Different stacking filters are applied, to enhance each base frequency, as each has a different  $h$  value.

The full process was applied to a two-second-long sweep of synthetic data that contains the sum of the three base frequencies, the powerline signal and a low frequency sinusoidal noise component with a period of 2 s, shown on Figure 11, with the respective power spectrum in Figure 12.

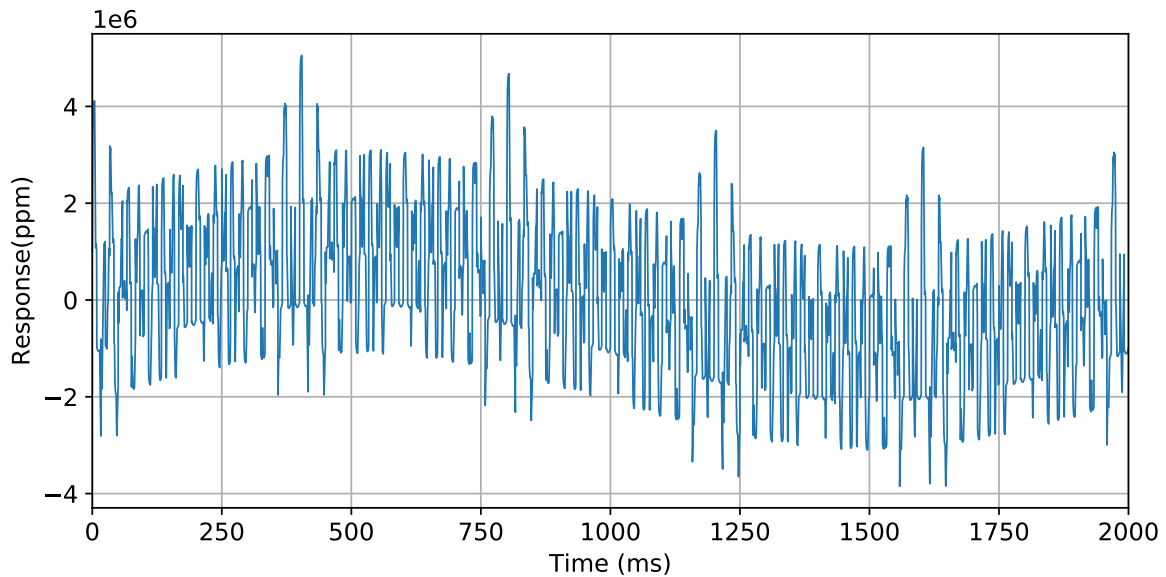


Figure 11: A 2000 ms combination of the 60 Hz powerline signal, the three source signals and a 0.5 Hz signal to simulate the movement of the device.

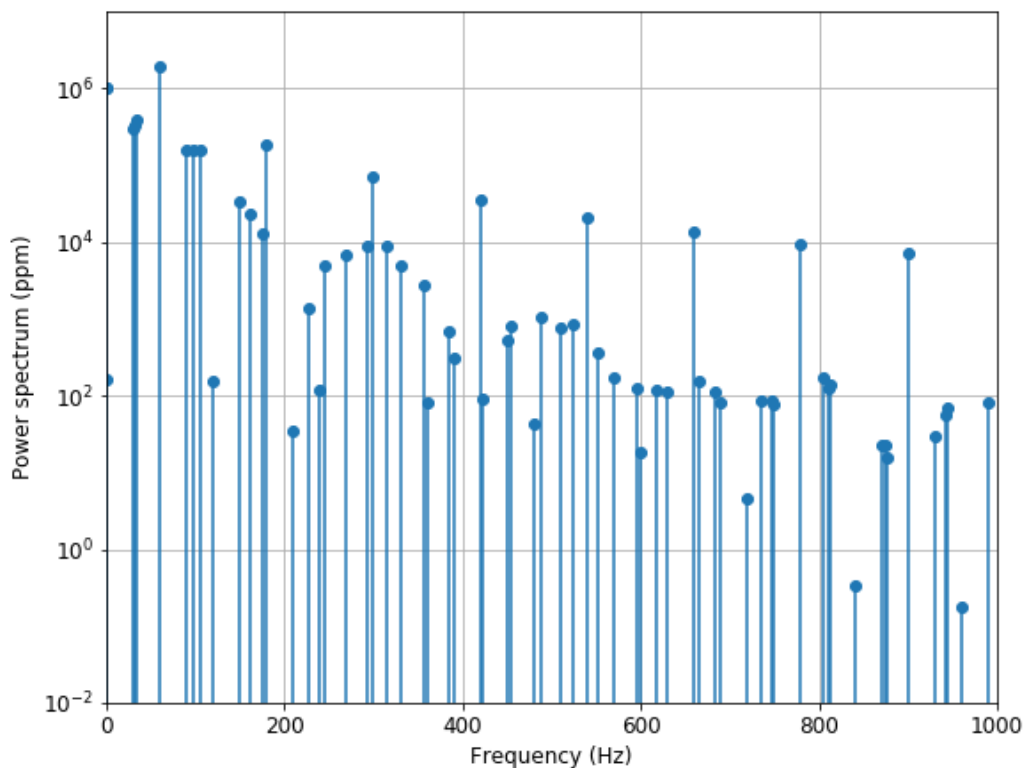


Figure 12: Zoomed in power spectrum for the mixed signal in Figure 11. Note only the odd harmonics for the source signals and all harmonics of the “dirty” powerline.

When comparing Figure 12 to Figure 10, it is evident that the frequency components of all the source signals, the low frequency noise and the “dirty” powerline are visible as expected. The increase in the magnitude of the power spectrum is a result of the whole time series being two seconds long compared with the single waveform spectrum shown in Figure 10.

The stacked results that were recovered, through using the Halverson Stacking process, are shown in Figure 13.

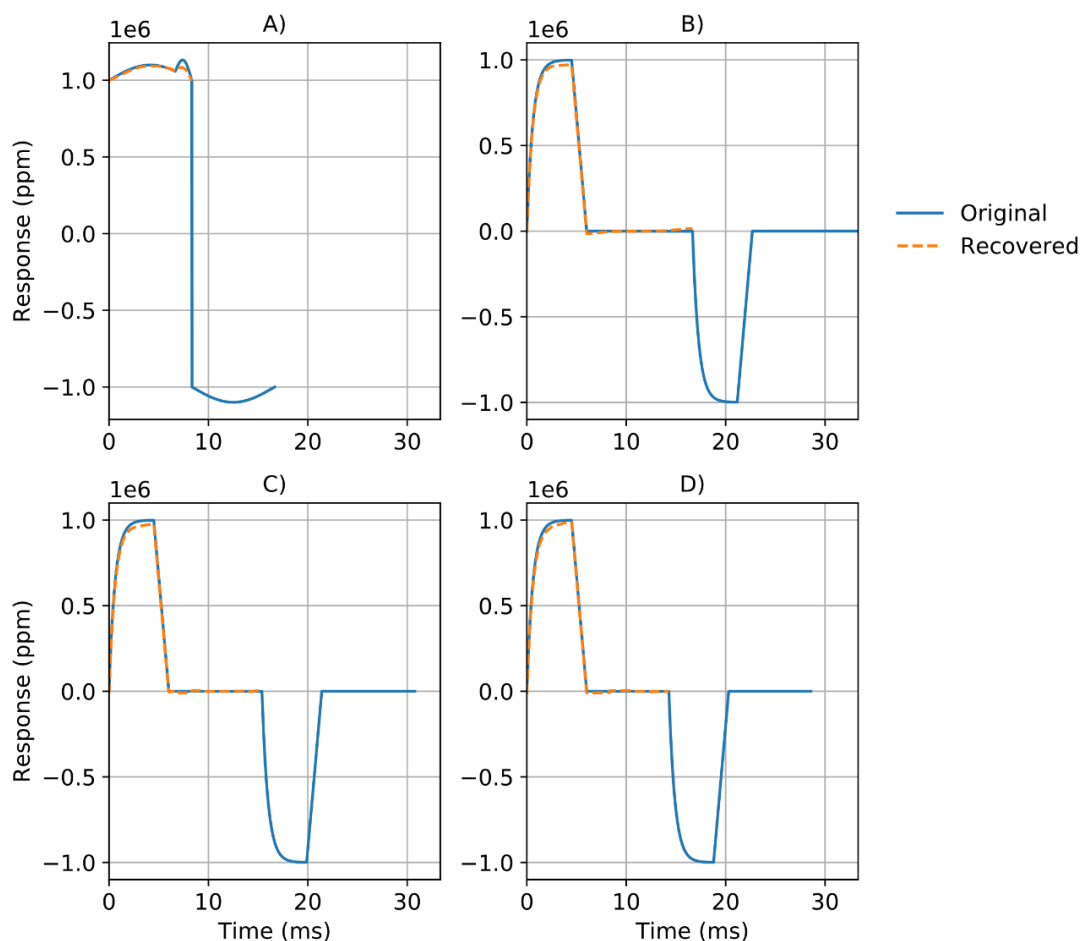


Figure 13: Results of applying a stacking analysis, dashed orange, compared to the original waveform, blue, A) 60 Hz powerline, B) 30 Hz signal, C) 32.5 Hz signal, D) 35 Hz signal.

Figure 13A shows the recovered powerline signal, orange dashed, and compares it to the original waveform (solid blue). There is a small discrepancy attributed to the asymmetric bump added at 7.5 ms and not added at approximately 15.8 ms. This bump was added to introduce even harmonics and the stacking filter removes these. When comparing the three source waveforms, it is noticed that they all have good recovery with the data, and within the 5% error of the original waveforms. Thus, the Halverson stacking filter is a good process to separate the signals of the 3CTx. Doubling the number of stacks, or increasing the signal duration to 4 seconds, gives the results shown in Figure 14.

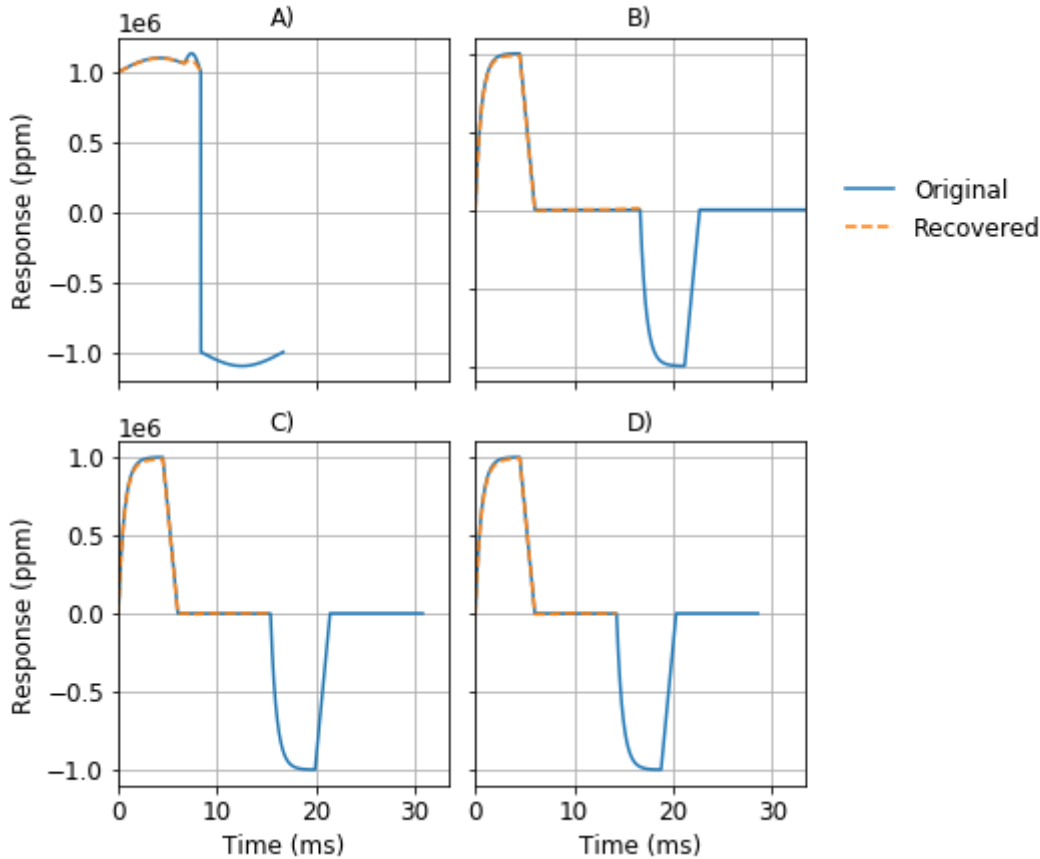


Figure 14: Results of apply the stacking analysis for 4s, dashed orange, compared to the original waveform, blue, A) 60 Hz powerline, B) 30 Hz signal, C) 32.5 Hz signal, D) 35 Hz signal.

Compared with Figure 13, the results on Figure 14 show a closer agreement to the expected three source signals of the 3CTx, with the maximum error being less than 2%. When the asymmetry evident in the powerline response is removed from Figure 14A, there is essentially no disagreement between the recovered and expected transmitter waveforms.

It is sometimes useful to estimate the low-frequency noise over a given sample interval. we noticed that the powerline, and the three source waveforms each had an integer number of complete cycles in a 0.4 second period, so that the sum of these signals had a pattern that repeated every 0.4 s (see Figure 11). Hence 0.4 s would be the minimum stacking period for this data. As the waveforms are bipolar, this means that when averaged over 0.4 seconds, each of

these four waveforms will have a mean of zero. Note, if a different set of frequencies are used this averaging period would be different.

However, the low-frequency waveform will not have a mean of zero over this period, so averaging the signal shown in Figure 11 over a 0.4 second period will remove the other signals and leave only the low-frequency signal. The average value over 0.4 second periods is plotted with x symbols on Figure 15 and compared with the original signal (blue solid line). The estimated values are within the 5% of the low-frequency noise, which is an acceptable accuracy for a noisy signal

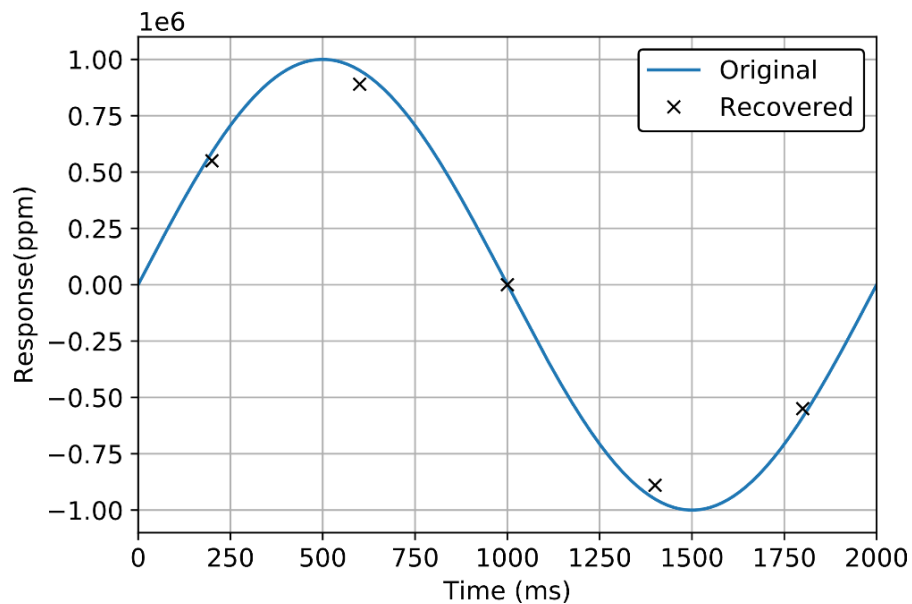


Figure 15: Estimation of the low frequency noise.

### 3.4 Conclusions for sets of base frequencies

We have selected three sets of base frequencies that might be suitable for a 3CTx. Set 1 contains the 15, 22.5, and 30 Hz base frequencies; Set 2 contains the 30, 32.5, and 35 Hz base frequencies; and set 3 contains 79, 97 and 113 Hz base frequencies. None of these three sets were found to have overlapping odd harmonics with each other or the odd and even harmonics of a powerline

signal. Set 3 contains odd harmonics separated by 1 Hz from the powerline frequencies, and would be appropriate where a high base frequency is suitable (e.g. in resistive ground). Set 1 has odd harmonics separated by 2.5 Hz from the powerline harmonics but has substantially different base frequencies, so these would show different responses for highly conductive bodies (Smith & Balch, 2000) and this would make comparison of the different components difficult. Set 2 also has odd harmonics separated by 2.5 Hz from the powerline harmonics and has similar base frequencies, so was selected for further analysis in this thesis. The base frequencies will ensure a moderate depth of exploration in conductive ground.

The Halverson stacking filter was able to separate the three base frequencies from each other, the powerline signal and low-frequency noise, with the the original waveform being recovered within a 5% error. Doubling the amount of stacking reduced the error for the source signals below 2%. Thus, illustrating that it is theoretically possible to separate the three transmitted fields that are combined into a summed response at a given receiver.

As a result, we have determined two of the necessary requirements for a 3CTx. We have defined frequency sets that could be used and a process that could be used to separate out the signals. In the next section forward, modelling will be done to see what impact the 3CTx frequencies will have on subsurface conductors with varying response parameters.

## Chapter 4

### Pulse shape and window selection

An important part of system or survey design is selecting appropriate pulse shape and window positions. We have used the wire-loop model developed by Grant and West (1965) to estimate the secondary field for different pulse/window configurations and a range of values of the response parameter of the wire-loop. We selected a total of eight representative windows with the first three windows being the off-time windows and the remaining five windows sampling the on-time. The on-time windows measure the response when the current is actively flowing through the transmitter coil. These on-time windows can be used to characterize excellent conductors, with larger values of  $\tau$ . The off-time windows occur after the primary field is no longer transmitting (Swift, 1988) and are used to characterize poorer conductors, indicated by lower values of  $\tau$ . The response measured in each window is averaged for each value of the response parameter,  $\tau$ . Two potential configurations are analyzed, 1) the pulse widths are fixed and the position of the windows relative to the pulse width is also fixed; and 2) the pulse width and window positions are scaled to be longer and later when the half-cycle is longer. The intention is to find a configuration where the response measured in each window can be compared and the differences will be small between different base frequencies. We estimated the differences as a function of frequency, and they showed a general linear dependence. Suggesting the base frequencies could be linearly combined to give the response that might be obtained at another frequency.

#### 4.1 Secondary Field Estimation

Models such as plates or spheres, are available in the literature (Annan, 1974; Lajoie & West, 1974; Nabighian & Macnae, 1991), but the calculation of the response can be complex (West &

Macnae, 1991). In many cases, the complex response can be approximated by the sum of several exponential decays, so the simple wire-loop model of Grant and West (1965) which has a simple exponential decay was used to rapidly estimate the secondary-field response of a subsurface conductor in the on-time and off-time (McNeill et al., 1984). As the more complex responses can be obtained by a linear combination of exponentials, analyzing the behaviour of a wire-loop will give a good indication of how more complex models will behave when excited by a 3CTx.

To model the results of the wire-loop model, Equation (13) was convolved with the frequency-domain representation of the three transmitter signals, for waveform configuration 1, where the pulse width does not change. The forward model somewhat arbitrarily assumed that the overall coupling from the transmitter to the receiver through the subsurface conductor was 0.33.

Increasing or decreasing this coupling will scale all the results up or down, but not change the relative differences between the different base frequencies. The time-domain representation of the secondary field associated with these signals can be seen below in Figure 16, for three significantly different values of the time constant,  $\tau$ , each representing different subsurface wire-loop conductors.

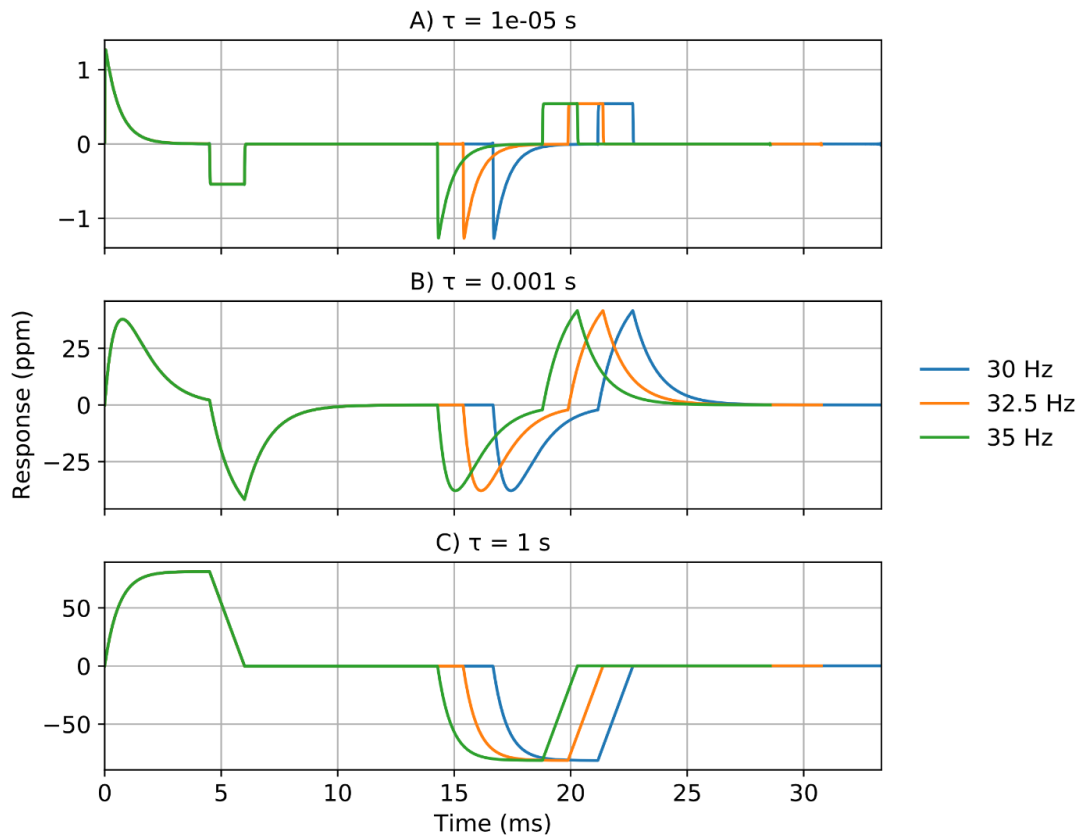


Figure 16: Time-domain conductor secondary field responses for an isolated conductor utilizing the Grant and West wire-loop model (1965), for waveform configuration 1, where the pulse widths are fixed and the position of the windows relative to the pulse width is also fixed

Figure 16, panel C) shows the case when the response parameter,  $\tau = 1$  s, a situation which is essentially at the inductive limit, as the secondary field is a scalar multiple of the primary signal. Such a situation is indicative of a “perfect conductor”, as the response is only significant in the on-time. Panel A) shows the case when  $\tau = 1 \times 10^{-5}$  s. In this situation the response parameter is small, near the resistive limit, and the secondary field in the frequency-domain is proportional to  $i\omega$ , so in the time-domain the secondary is the derivative of the original waveform. This situation is characteristic of a “weak conductor” and once again, there is only a significant response in the on-time. Panel B) shows the case between these two limits, when  $\tau = 0.001$  s and shows the secondary field response for a conductor with a response observable in the off-time.

In order to capture all these situations, it is necessary to have measurement windows appropriately placed in the on-time and off-time windows.

## 4.2 Windowing

We calculated the response of wire-loop model with response parameters between  $1 \times 10^{-5} \leq \tau \text{ (s)} \leq 1$  and investigated the impact of changing the pulse length and the window widths for the three frequencies from Set 2. The intent is to see which pulse length and window positions and widths gives the responses which are least impacted by changing the base frequency. For simplicity, we will term a pulse length and corresponding set of window positions and widths the “waveform configuration”.

Two different waveform configurations were looked at in this analysis. We primarily focused on the off-time windows as these are the windows most commonly analyzed. The first waveform configuration, configuration 1, is illustrated in Figure 17. For each frequency, the pulse width is 6 ms and the three off-time windows (W1, W2, and W3), are placed with W1 starting 0.5 ms after the pulse ends to limit the amount of noise associated with the end of the pulse. Each subsequent off-time window (W2 and W3) starts as soon as the previous window ends and is twice as wide as the previous window, as widths usually increase at later delay times (Nabighian & Macnae, 1991). Five on-time windows were created, Window 4 is for when the exponential ramp on is more linear, Window 5 is for the curved section of the ramp on, and Window 6 is when the waveform is constant. The linear ramp turn off is split equally between Windows 7 and 8.

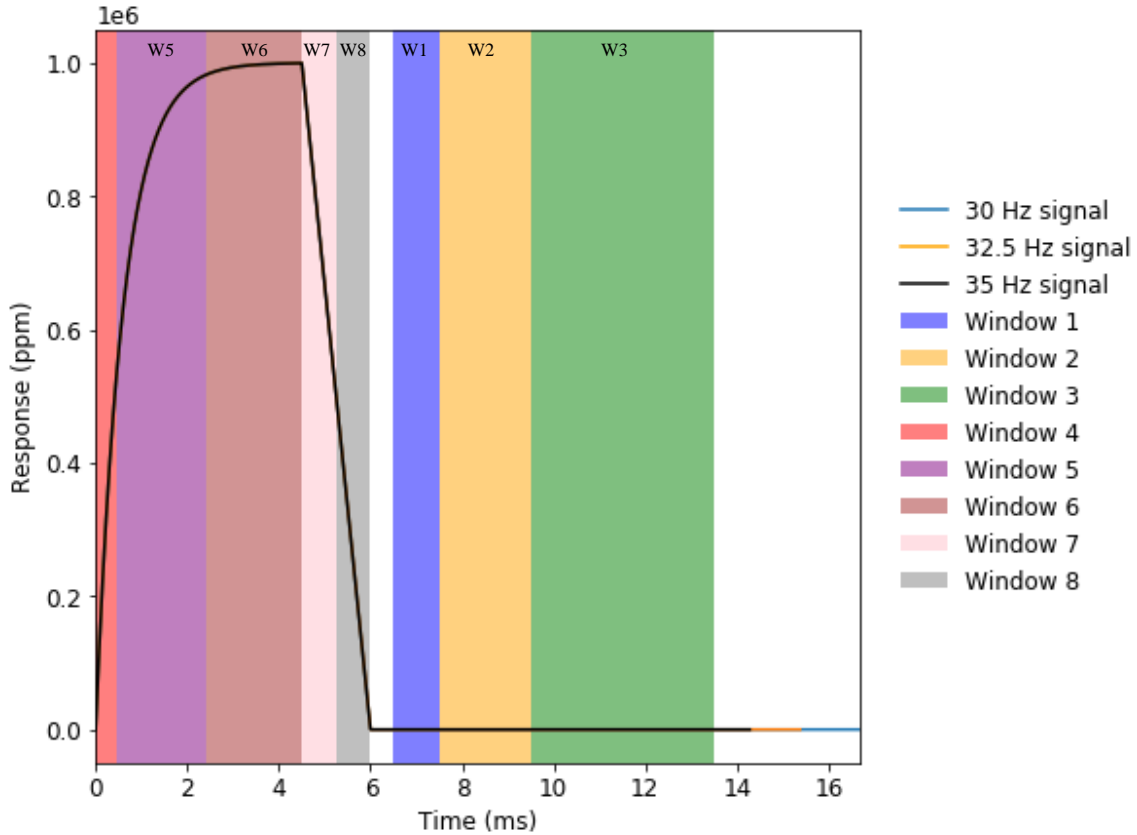


Figure 17: All window locations for equal 6 ms pulse widths and fixed window positions, for the three base frequencies, where the on-time and off-time windows are identical. Note the labels at the top of the diagram refer to the respective window, for example W3 refers to Window 3.

The windowed response was calculated as function of different values of  $\tau$  and then normalized by the peak response, and plotted in Appendix A. The curves for each base frequency look very similar, so we have calculated the difference using

$$Diff = R_2 - R_1, \quad (27)$$

where,  $Diff$  is the difference array,  $R_1$  is the smaller base frequency, and  $R_2$  is the larger base frequency. The responses (in ppm) as a function of  $\tau$  for waveform configuration 1 can be found below in Figure 18 with three curves for the three base frequencies.

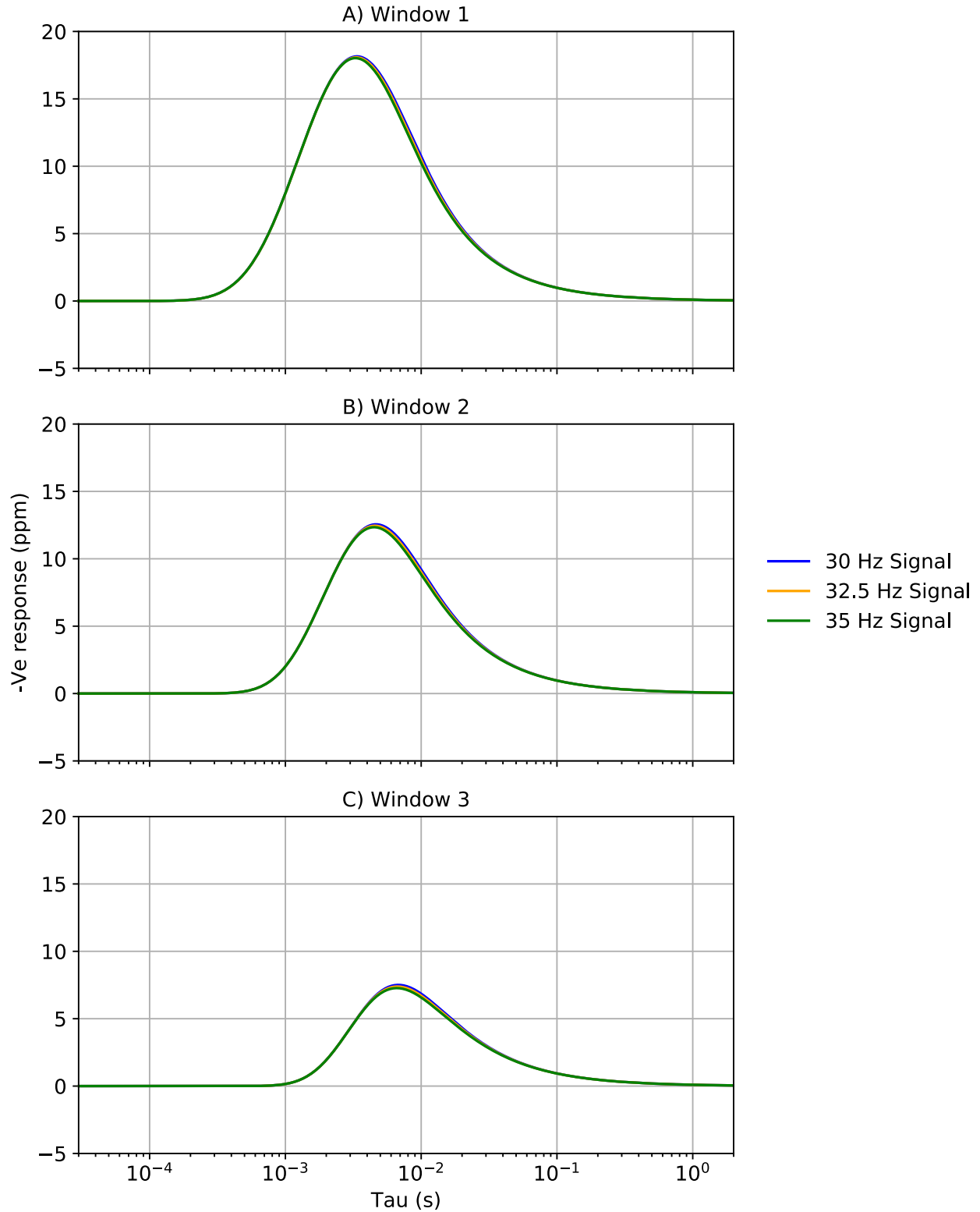


Figure 18: Windowed data results for the window locations from Figure 17 as a function of the  $\tau$  value, A) Window 1, B) Window 2, C) Window 3.

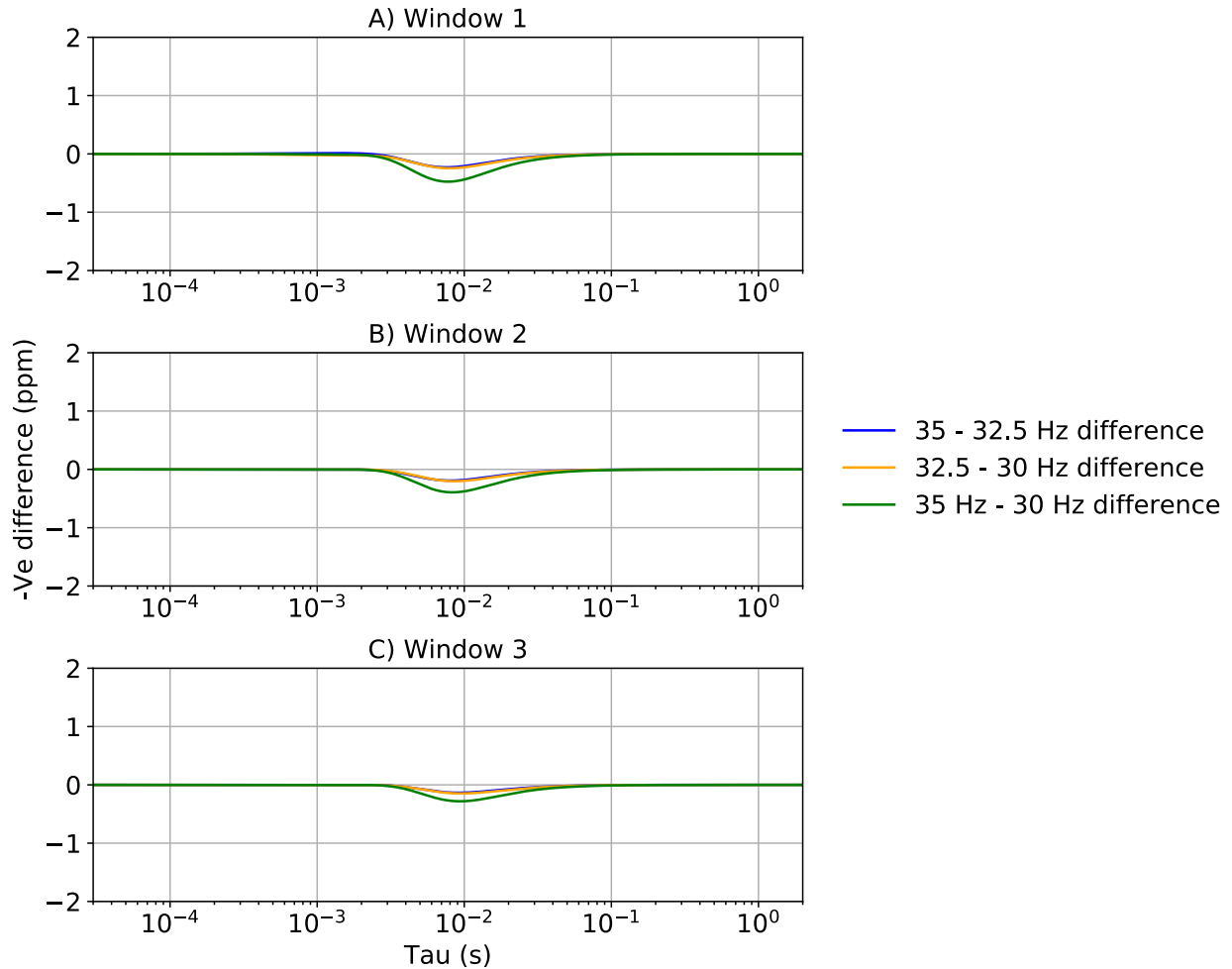


Figure 19: Windowed data differences for the window locations from Figure 17 as a function of the  $\tau$  value, A) Window 1, B) Window 2, C) Window 3.

The responses are very similar as they plot on top of each other, with the lower frequencies largely overlain by the 35 Hz response (green curve). These responses vary over a large range and when plotted on a linear scale, it is difficult to see small differences. The actual differences plotted on Figure 19 are about two or more orders of magnitude lower than the responses. For example, the largest difference in window 1 at the 35 Hz and 30 Hz base frequencies occurs close to  $\tau = 0.008$  s where the difference has a maximum of approximately 0.476 ppm, the actual response is close to 15 ppm, so the normalized difference is about 3%.

To contrast these results, the same methodology was applied to waveform configuration 2 where the pulse widths and window positions and widths were decreased by a reduction factor, R.F. given by

$$R.F. = \frac{\text{component base frequency}}{30\text{Hz}}. \quad (28)$$

Using this factor, the 30 Hz component windows remain unchanged, but the 32.5 Hz component windows are reduced by a factor of 1.09 and the 35 Hz component windows are reduced by a factor of 1.17. The pulse widths of the waveforms in this case were reduced by the same R.F. as the windows were. A graphical representation of how the pulse and windows change can be seen below in Figure 20, and the peak normalized response as a function of  $\tau$  is found in Appendix B.

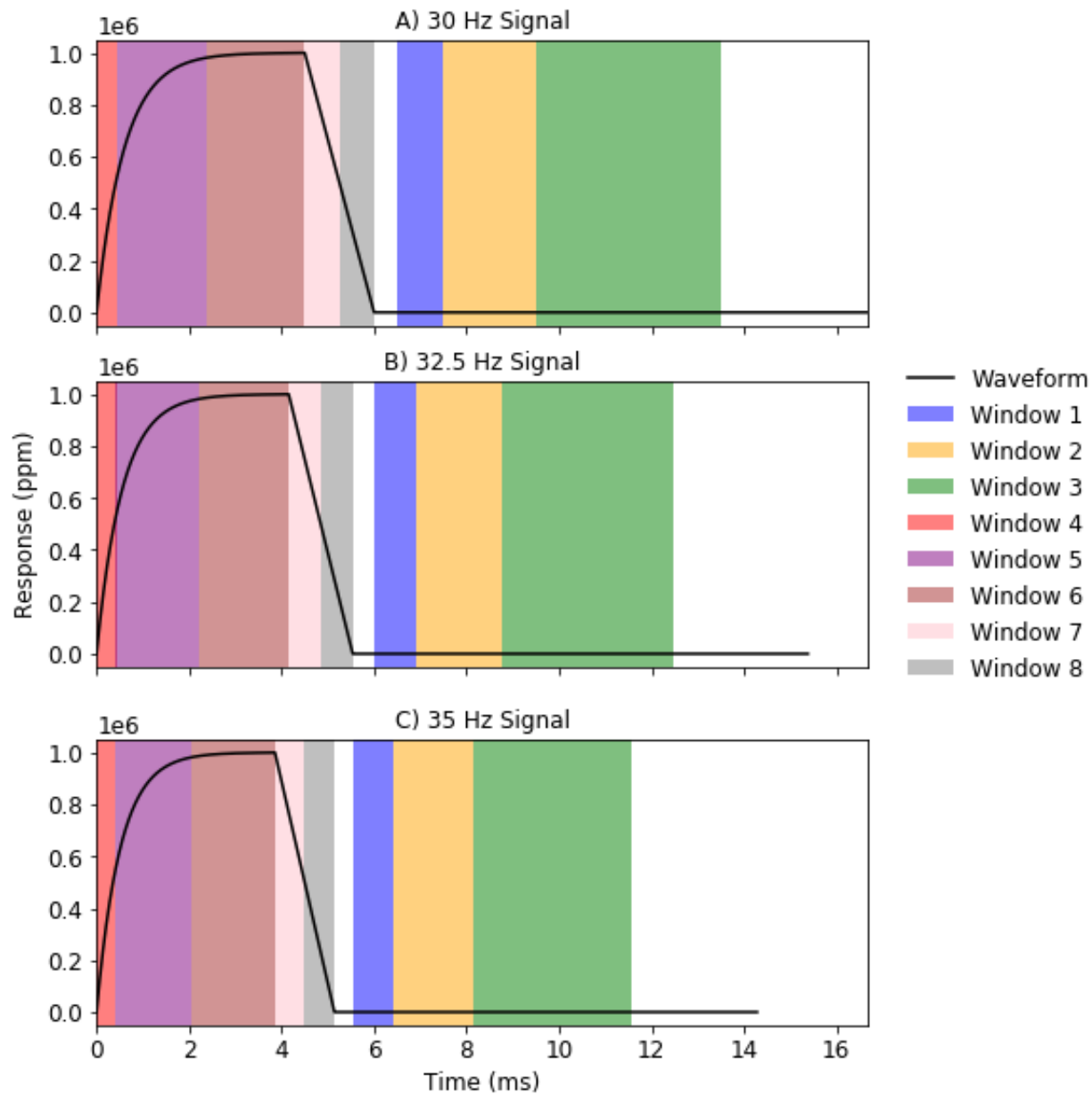


Figure 20: All window locations and pulse widths varied by the reduction factor, resulting in smaller window widths for larger base frequencies, A) 30 Hz signal, B) 32.5 Hz signal, C) 35 Hz signal.

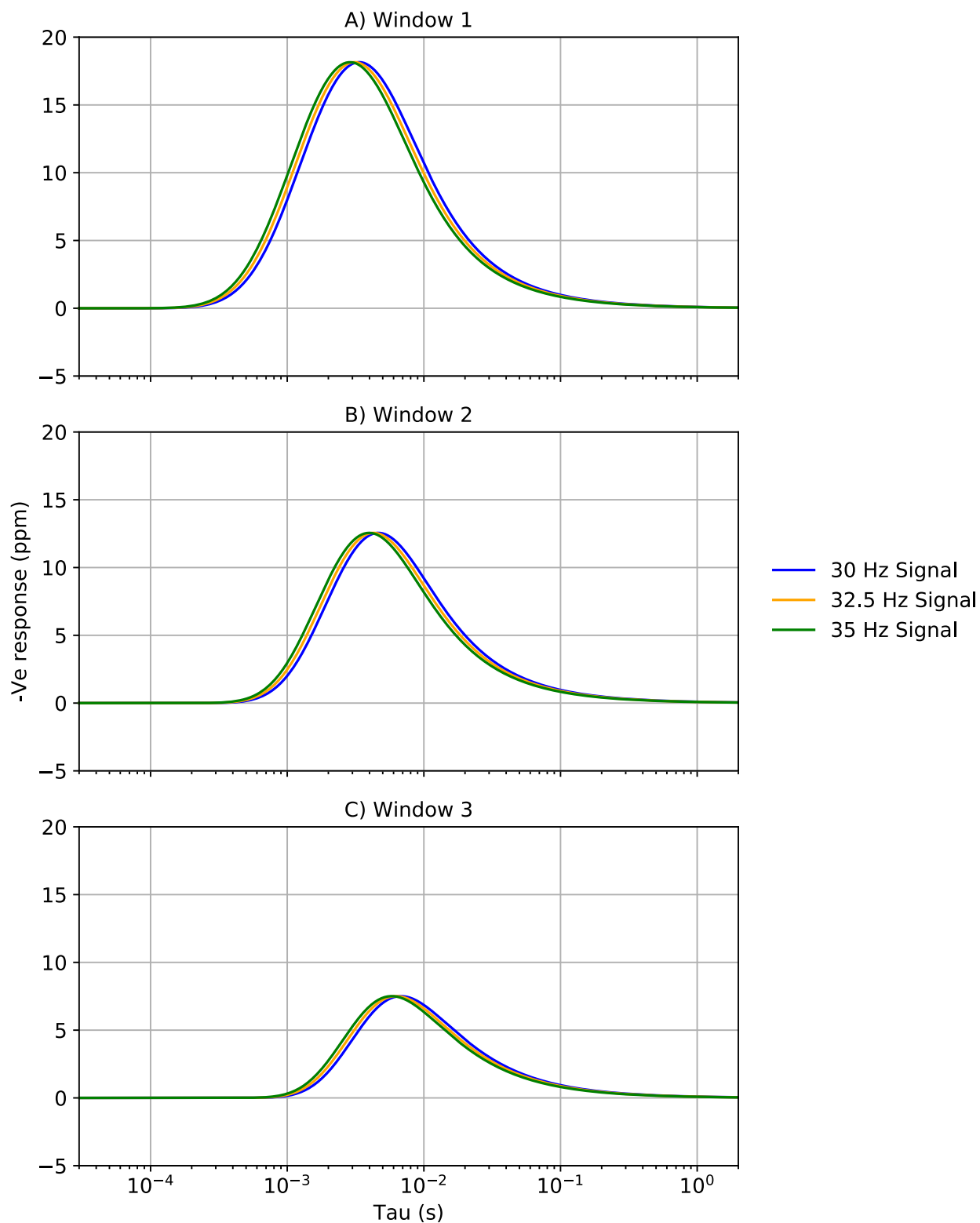


Figure 21: Windowed data results for the window locations from Figure 20 compared to the  $\tau$  value, A) Window 1, B) Window 2, C) Window 3.

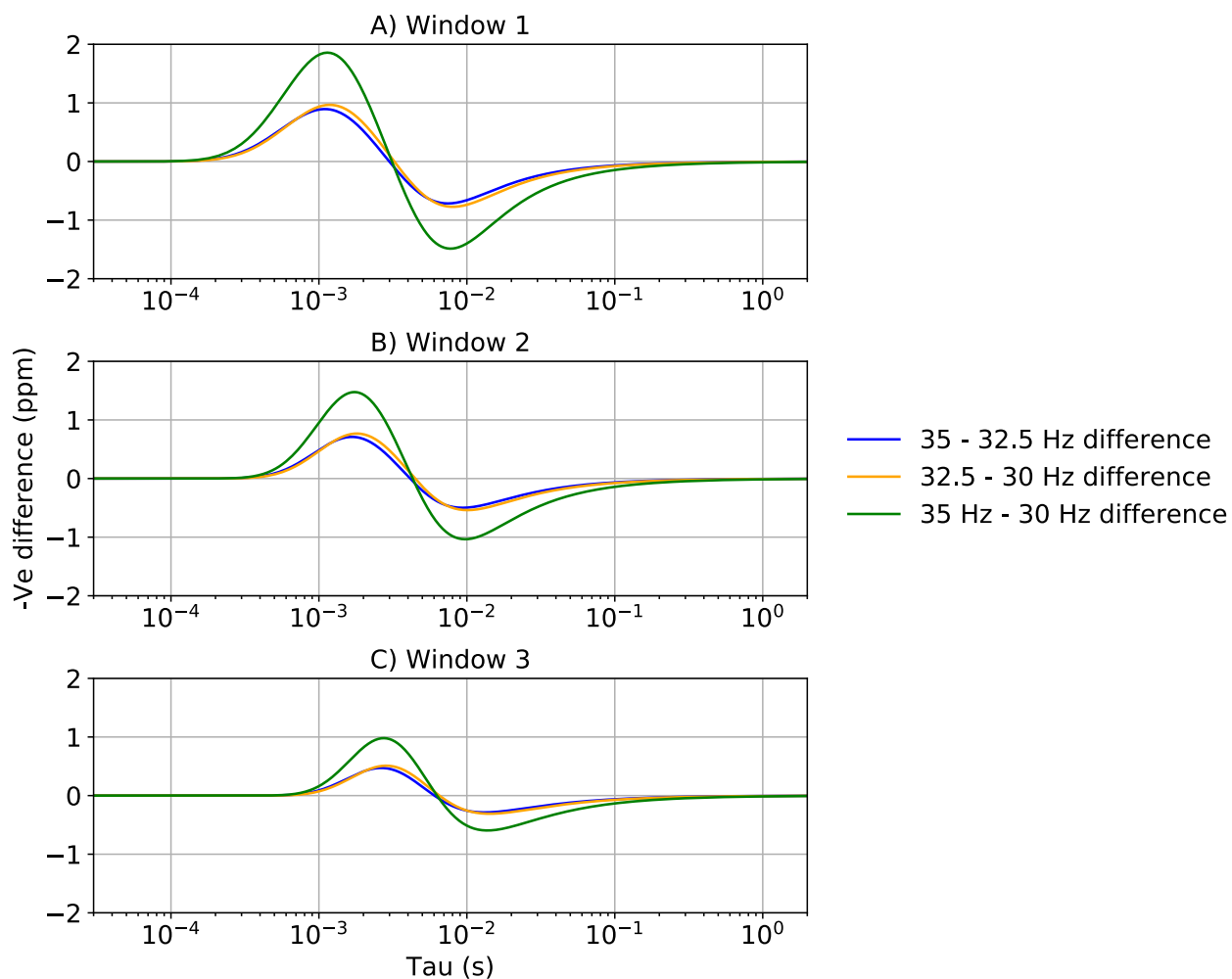


Figure 22: Windowed data differences for the window locations from Figure 20 compared to the  $\tau$  value, A) Window 1, B) Window 2, C) Window 3.

Figure 21 shows the windowed response and Figure 22 shows the differences as a function of  $\tau$  for the off-time windows of waveform configuration 2. The responses do not plot as closely over each other and the maximum differences between the individual windows occur in Window 1 with an estimated difference of 1.857 ppm, when the responses are about 15 ppm, representing a difference of 12%. At lower values of  $\tau$ , or a poor conductor situation, the relative differences are larger.

When comparing the response differences of the off-time windows, as seen in Figure 19 and Figure 22, there is clearly a larger separation between the curves representing the scaled window

widths and the curves for the fixed window widths. Generally, the differences are about a factor of five, larger for the scaled waveform. In the case of the 3CTx we want these differences to be as small as possible so we can compare and combine the responses from the different components acquired using the different base frequencies. Hence, we determined that using the same on-time and off-time window widths were the best method for the three frequencies of the 3CTx.

To understand if the differences were predictable as a function of frequency, we calculated the difference between each window at a given value of  $\tau$ . Note that the frequencies we compared were spread around the 30 Hz base frequency with differences up to 33% from the 30 Hz base frequency. The results of this difference analysis can be found below in Figure 23, where the three panels show the difference for the three windows at three different  $\tau$  values. Note, that the last 3 frequency combinations (>25% difference) were omitted from window 3, Graph C), because the window width began to overlap into the next half-pulse of the waveform. Making it an invalid situation to analyze.

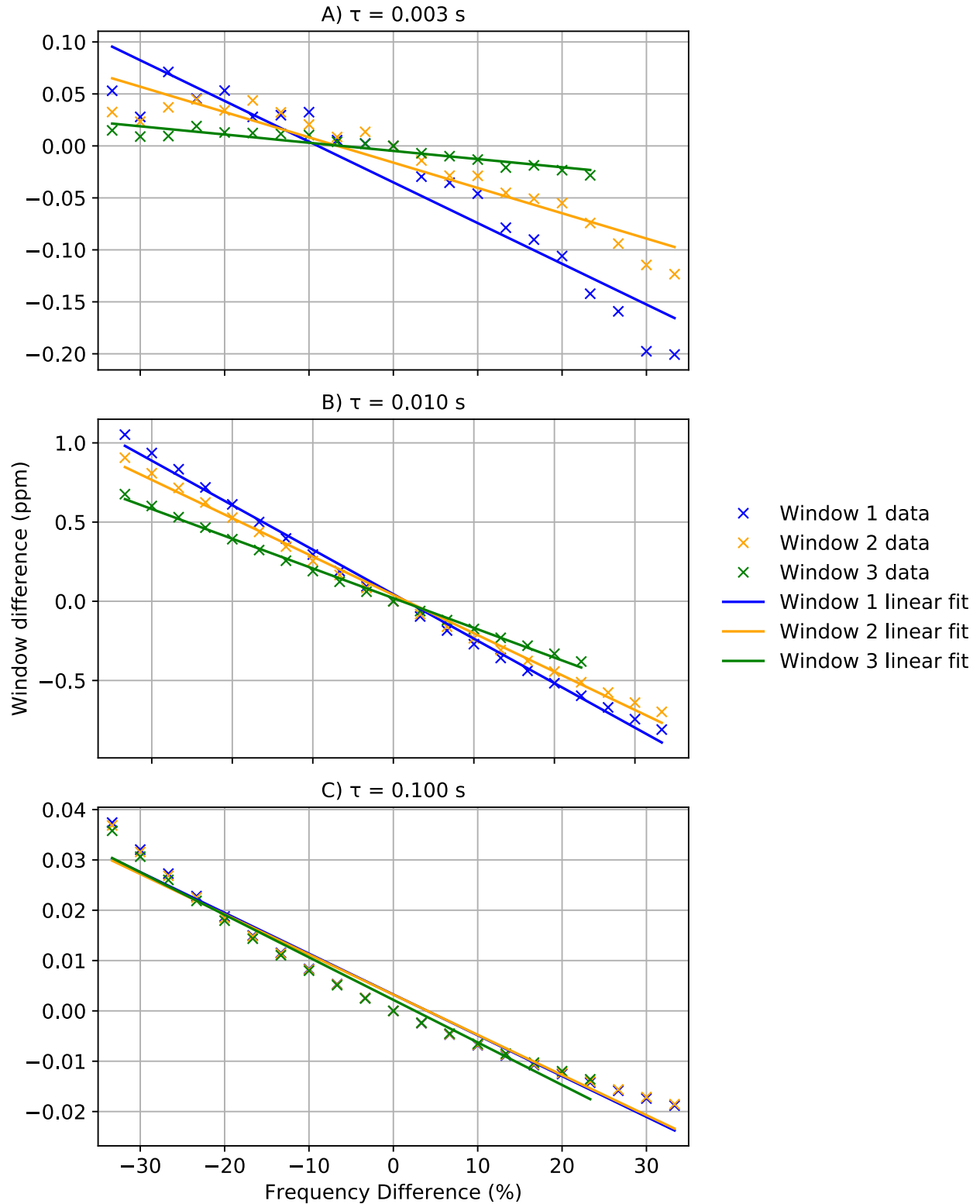


Figure 23: Window differences by varying the base frequencies for the equal pulse width waveform for the off-time windows.

When the difference in the base frequencies is small, e.g., 10%, then the amplitude difference will be small, so the responses from different transmitters could be compared with only small errors. Furthermore, the differences appear linear, with the correlation coefficients shown in Table 2.

Table 2: Coefficient of Correlation for the linear regression performed in Figure 23.

$\tau$ (s)	Window	Coefficient of Correlation ( $R^2$ )
<b>0.003</b>	Window 1	0.904
	Window 2	0.897
	Window 3	0.883
<b>0.010</b>	Window 1	0.995
	Window 2	0.995
	Window 3	0.997
<b>0.100</b>	Window 1	0.966
	Window 2	0.966
	Window 3	0.973

The lowest  $R^2$  value is 0.883, which occurs in Window 3 when  $\tau = 0.003$  s. In this case, the poor correlation is not critical as the maximum difference is less than 0.02 ppm. Otherwise, a reasonable fit can be obtained using a linear function, particularly for the decays typically measured and for small changes in frequency, but if greater accuracy is required, a polynomial fit could be used. These results indicate that the differences and hence the responses vary in a linearly predictable way. Furthermore, the actual response at certain base frequencies could be scaled to give the same response as if another base frequency were used and then the small errors

could be reduced. This will be useful if we want to generate linear combinations of responses from transmitters in different orientations, as proposed by Smith (2012) and Smith (2018).

One way of scaling the responses would be to switch frequencies in a specific transmitter component and then combine the results. For example, say the vertical transmitter is always operating at 32.5 Hz. The horizontal north component transmitter could operate at 30 Hz for a certain amount of time while the horizontal east component transmitter operated at 35 Hz. Then after a certain amount of time, the north and east component would switch base frequencies. The 30 and 35 Hz base frequency amplitudes could then be linearly combined to give the response as if all transmitters were operating at 32.5 Hz.

By taking the mathematical average of the 30 Hz signal and the 35 Hz signal that are shown on Figure 18, we produced what we referred to as the 32.5L Hz signal. Equation (27) was then applied to determine the difference between the 32.5 L Hz and the 35 Hz signals. The difference between the 32.5L Hz and 32.5 Hz signals are shown on Figure 24, in combination with the differences from Figure 19, for comparison.

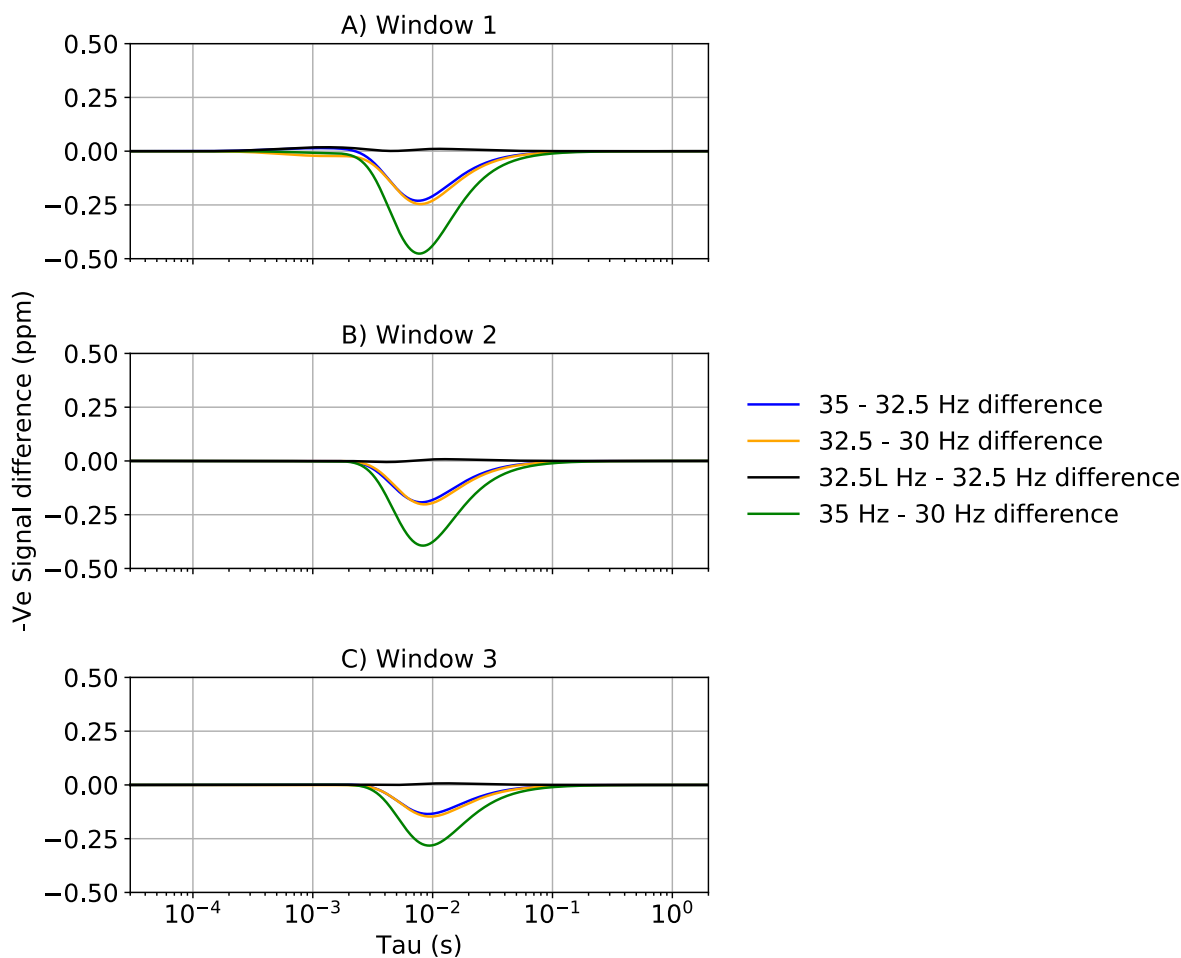


Figure 24: Plotting the differences for the differences between the frequencies. In addition, the difference between the estimated 32.5 Hz response and the 32.5 Hz response.

Analysing the results, you can see that for all three off-time windows, for waveform configuration 1, the difference for the 32.5L Hz frequency is much less than the others, with the largest difference being 0.02 ppm. As a result, it can be concluded that multi component data can be linearly combined to create data as if it was operating at one frequency. This will allow a single coil 3CTx to collect data, using all three base frequencies. These could be reasonably corrected to the response at a single frequency, and mathematically combined as originally purposed in Smith (2012) and Smith (2018).

### 4.3 Conclusions for waveform configurations

The wire-loop model was used to predict the responses for different base frequencies, pulse widths and window configurations. It was found that when the pulse shape and windows were fixed (waveform configuration 1), the variation of the window response with base frequency was less than when the pulse width and window positions were scaled by a reduction factor (waveform configuration 2). In the case of the 3CTx we want these differences in the window response to be as small as possible, leading us to determining that waveform configuration 1 with equal pulse widths and windows starting and ending at the same time after the end of the pulse are the most suitable windowing method for the 3CTx.

Later modelling of waveform configuration 1 showed that the response of each of the off-time windows could be estimated using a linear trend line. This implied that the response in one transmitter could be estimated at a frequency that is similar to the frequencies in another transmitter with minimal error, making the data directly comparable. This was demonstrated by estimating the 32.5 Hz windows by taking the average of the 30 Hz and 35 Hz windows. This would require that one or more transmitters switch between two base frequencies during a survey. In conclusion, when the base frequency varied, the differences plotted along a linear trend indicating that the errors caused by varying the frequencies are predictable and could be corrected.

## Chapter 5

### Final Conclusions

The 3CTx EM surveying is an innovative mineral exploration tool. The three components are orthogonal and co-located, with each component emitting a field that excites the subsurface. The three resulting secondary fields will be measured by receivers during a geophysical survey.

We have proposed three sets of potential base frequencies for the 3CTx, one set (15, 22.5 and 30 Hz) would be suitable for conductive ground, another set (79, 97 and 113 Hz) would be suitable for more resistive ground and 30, 32.5 and 35 Hz, would be suitable for intermediate cases. We confirmed that for the latter case a stacking filter could be used to separate the signals. Modelling the wire-loop response from these three base frequencies and calculating the difference for multiple subsurface conductors, with different decay characteristics, allowed us to understand how the response varied for different windows and pulse configurations. Two potential configurations are analyzed, 1) the pulse widths are fixed and the position of the windows relative to the pulse width is also fixed; and 2) the pulse width and window positions are scaled to be longer and later when the half-cycle is longer. As the smaller differences occurred in configuration 1 it is recommended to use similar pulse widths and window configurations. Hence responses from these three base frequencies can be approximately compared. If more accurate comparisons are required, it is possible to linearly interpolate or extrapolate the responses of the 3CTx to estimate the response at a different base frequency. This is possible as each of the off-time windows show a strong linear dependence with frequency for all windows and a wide range of decay rates. This was demonstrated by showing that a response extremely close to a 32.5 Hz response could be obtained through averaging the 30 Hz and 35 Hz signals. This would require the transmitters to switch frequencies for each orientation.

We have therefore defined many of the system parameters of a 3CTx system. To confirm that this system is a practical device, it requires that a prototype be constructed. During this process, the testing can be used to show if the desired waveform can be reasonably constructed in each of the coils. Additionally, the testing will investigate if there is any interference between the transmitter coils and if there is, how it might be reduced.

Upon completion of the laboratory testing, we suggest that the first field test to be completed over a well-known ore body. This could be used to demonstrate if there are improvements to the signal-to-noise ratio when compared to a 1CTx, something difficult to test synthetically. An improved signal-to-noise ratio would allow better mapping of subsurface conductors at greater depths. In the case an improved signal-to-noise ratio is not achieved, more laboratory testing may be necessary to refine the prototype. The ultimate objective would be 3CTx system that could become a valuable exploration tool that would aid in the discovery of ore deposits, such as those in Sudbury.

## Bibliography

- Annan, A. P. (1974). The equivalent source method for electromagnetic scattering and its geophysical application. *PhD thesis*.
- Becker, A., & Cheng, G. (1987). Detection of Repetitive Electromagnetic Signals. In M. N. Nabighian, & J. D. Corbett, *Electromagnetic Methods in Applied Geophysics - Theory* (pp. 442-467). Society of Exploration Geophysicists. <https://doi.org/10.1190/1.9781560802631.ch7>
- Bracewell, R. (2000). *The Fourier Transform and Its Applications* (3rd ed.). McGraw Hill.
- Burger, H. R., Sheehan, A. F., & Jones, C. H. (2006). *Introduction to Applied Geophysics: Exploring the Shallow Subsurface*. New York: W. W. Norton & Compnay, Inc.
- Buselli, G., & Cameron, M. (1996). Robust statistical methods for reducing sferics noise contaminating transient electromagnetic measurements. *Geophysics*, *61*(6), 1633–1646. <https://doi.org/10.1190/1.1444082>
- Desmarais, J. K., & Smith, R. S. (2016). Benefits of using multi-component transmitter-receiver systems for determining geometrical parameters of a dipole conductor from single-line anomalies. *Exploration Geophysics*, *47*(1), 1–12. <https://doi.org/10.1071/EG14076>
- Gisselø, P. G. (2018). SkyTEM312HP – Optimized for depth of investigation. *International Workshop on Airborne Electromagnetics*, 1–2.
- Grant, F. S., & West, G. (1965). *Interpretation Theory in Applied Geophysics*. New York: McGraw-Hill Book Company.
- Griffiths, D. J. (2013). *Introduction to Electrodynamics*, 4th edition. Pearson.
- Hodges, G., & Chen, T. (2015). Geobandwidth: Comparing time-domain electromagnetic waveforms with a wire-loop model. *Exploration Geophysics*, *46*(1), 58–63. <https://doi.org/10.1071/EG14032>
- Kingman, J. E., Halverson, M., & Garner, S. J. (2004). *Stacking of Controlled Source Electrical Geophysical Data*. Retrieved from Terrigena Technical White Paper Number 20040328.0101(e): <https://citeseerx.ist.psu.edu/viewdoc/download?doi=10.1.1.486.435&rep=rep1&type=pdf>
- Kolaj, M., & Smith, R. (2014). A multiple transmitter and receiver electromagnetic system for improved target detection. *Society of Exploration Geophysicists International Exposition and 84th Annual Meeting SEG 2014*, *80*(4), 1754–1758. <https://doi.org/10.1190/segam2014-0133.1>
- Konieczny, G., Miles, P., & Smiarowski, A. (2016). Breaking through the 25/30 Hz barrier: Lowering the base frequency of the HELITEM airborne EM system. *SEG Technical Program Expanded Abstracts*, *35*(1998), 2218–2222. <https://doi.org/10.1190/segam2016-13957502.1>

- Lajoie, J. J., & West, G. F. (1974). The electromagnetic response of a conductive inhomogeneity in a layered earth. *Geophysics*, *41*, 1133-1156.
- Lee, J. B., Turner, R. J., Downey, M. A., Maddever, A., Dart, D. L., Foley, C. P., Binks, R., Lewis, C., Murray, W., Panjkovic, G., & Asten, M. (2001). Experience with SQUID magnetometers in airborne TEM surveying. *Exploration Geophysics*, *32*(1), 9–13. <https://doi.org/10.1071/EG01009>
- Lymburner, J., & Smith, R. S. (2015). A procedure for collecting electromagnetic data using multiple transmitters and receivers capable of deep and focused exploration. *Geophysics*, *80*(1), E1–E10. <https://doi.org/10.1190/GEO2014-0251.1>
- Macnae, J. (2017). Advances in Electromagnetic Data Processing: Noise, Signal, SPM and AIP. *Proceedings of Exploration 17: Sixth Decennial International Conference on Mineral Exploration*, 191–208.
- Macnae, J. C., Lamontagne, Y., & West, G. F. (1984). Noise processing techniques for time-domain EM systems. *Geophysics*, *49*(7), 934-948. <https://doi.org/10.1190/1.1441739>
- Mcfadden, P. L., & Kravis, S. (1986). The Nth-root stack: Theory, applications, and examples. *Geophysics*, *51*(10), 1879–1892.
- McNeill, J. D., Bosnar, M., & Levy, G.M. (1984). Application of simple loop models to the interpretation of transient EM surveys in a resistive environment. In *Geonics Limited Technical Note* (Issue TN-12).
- Nabighian, M. N., & Macnae, J. C. (1991). TEM Prospecting Methods. In M. N. Nabighian & J. D. Corbett (Eds.), *Electromagnetic Methods in Applied Geophysics - Applications Part A and Part B*, 427–520. Society of Exploration Geophysicists.
- Oliphant, T. E. (2006). *Guide to Numpy*. Retrieved from Internet Archive: <https://archive.org/details/NumPyBook/n3/mode/2up?q=Fourier>
- Rudd, J., Sharpe, R., Ritchie, T. J., & Barrett, J. (2017). Electrical Geophysical Systems – Review and Outlook. *Proceedings of Exploration 17: Sixth Decennial International Conference on Mineral Exploration*, 183–190.
- Shatkey, H. (1995). The Fourier Transform - A Primer. In *Department of Computer Science - Brown University* (Issue November). <http://cs.brown.edu/research/pubs/techreports/reports/CS-95-37.html>
- Smiarowski, A. (2012). *Detection of Perfectly-Conducting Targets with Airborne Electromagnetic Systems*. [University of Toronto, Toronto, Canada]. <https://doi.org/10.1017/CBO9781107415324.004>
- Smith, R.S. (2012). *Canada Patent No. CA2829617A1*.

- Smith, R. S. (2018). An airborne electromagnetic system with a three-component transmitter and three-component receiver capable of detecting extremely conductive bodies. *Geophysics*, 83(5), E347–E356. <https://doi.org/10.1190/geo2017-0849.1>
- Smith, R.S., & Balch, S.J., (2000). Robust estimation of the band-limited inductive-limit from impulse-response TEM measurements taken during the transmitter switch-off and the transmitter off-time: Theory and an example from Voisey's Bay, Labrador, Canada. *Geophysics*, 65, 476-481. <https://doi.org/10.1190/1.1444741>
- Strauss, W. (2000). Digital signal processing. In *IEEE Signal Processing Magazine* (Vol. 17, Issue 2). <https://doi.org/10.1109/79.826412>
- Swift, C. M. (1988). Fundamentals of the Electromagnetic Method. In M. N. Nabighian (Ed.), *Electromagnetic Methods in Applied Geophysics - Theory Volume 1* (pp. 4–11). Society of Exploration Geophysicists. <https://doi.org/10.1190/1.9781560802631.ch1>
- Watts, A. (1997). Exploring for nickel in the 90's, or 'til depth us do part'. In A. G. Gubins, (Ed.), *Proceedings of Exploration 97: Fourth Decennial International Conference on Mineral Exploration*, 1003–1014.
- West, G. F., & Macnae, J. C. (1991). APPLIED GEOPHYSICS--APPLICATIONS Part METHODS. In M. N. Nabighian (Ed.), *Electromagnetic Methods in Applied Geophysics - Applications Part A and Part B* (pp. 5–45). Society of Exploration Geophysicists.

## Appendices

### A Windowed analysis for waveform configuration 1

Figure 25, Figure 26 and Figure 27 are the windows responses as a function of  $\tau$  for the three base frequencies, 30, 32.5 and 35 Hz under waveform configuration 1. The off-time responses (panel A) are very small for small  $\tau$ , increase to a peak between  $\tau = 10^{-2}$  and  $10^{-3}$  and then decrease with amplitudes inversely proportional to  $\tau$ . For small  $\tau$  the on-time responses (panel B) increase linearly, with  $\tau$  and are also proportional to the slope of the time derivative of the waveform. As window 4 has the steepest slope it has the largest response. As  $\tau$  increases the on-time responses level off to be roughly constant in the inductive limit. The plots for each frequency appear very similar to the plot for the other frequency. Hence in the main text we look at the differences of each plot.

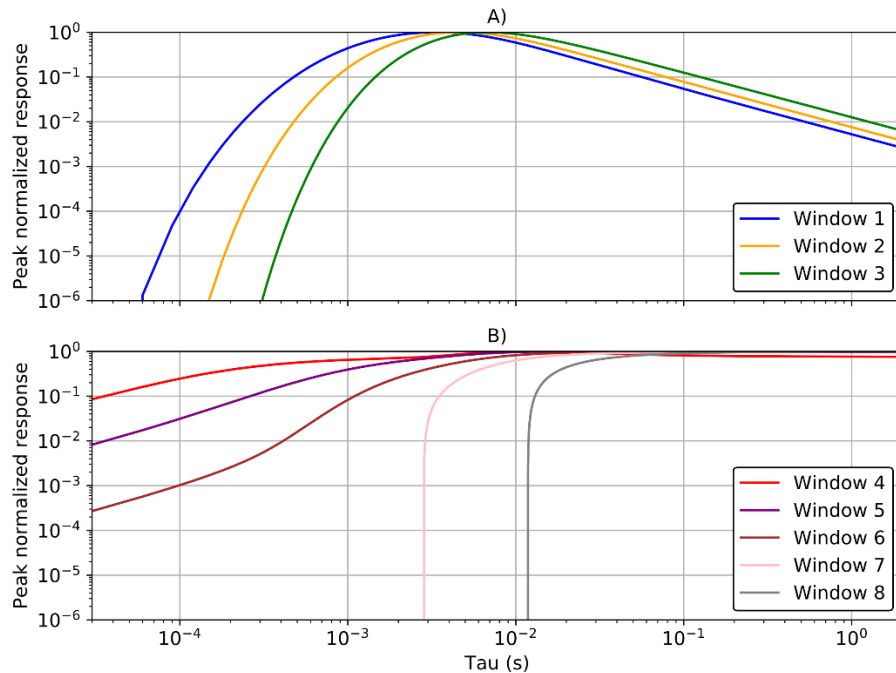


Figure 25: Peak normalized window response as a function of  $\tau$ , for the 30 Hz signal with a 6 ms pulse width A) off-time B) on-time

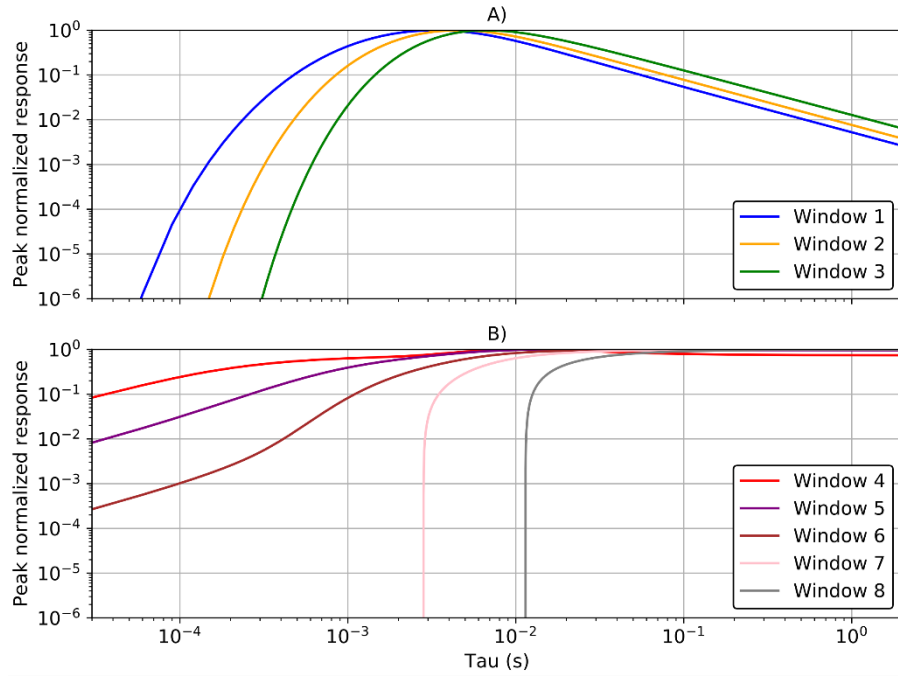


Figure 26: Peak normalized window response as a function of  $\tau$ , for the 32.5 Hz signal with a 6 ms pulse width A) off-time B) on-time

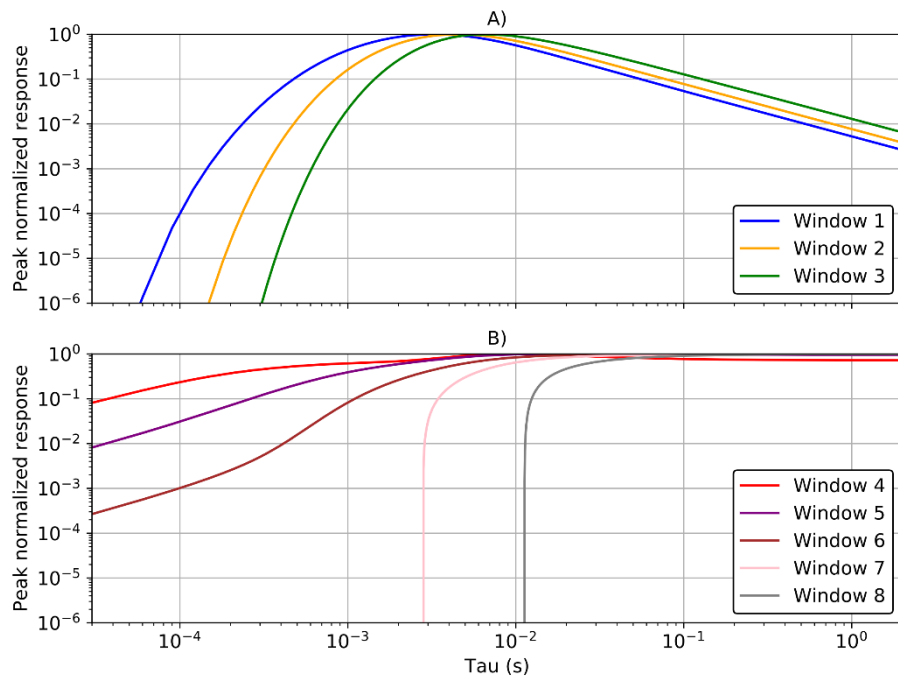


Figure 27: Peak normalized window response as a function of  $\tau$ , for the 35 Hz signal with a 6 ms pulse width A) off-time B) on-time

## B Windowed analysis for waveform configuration 2

Figure 28, Figure 29 and Figure 30 are the windows responses as a function of  $\tau$  or the three base frequencies, 30, 32.5 and 35 Hz under waveform configuration 2. In general, the plots for the three base frequencies appear very similar to each other and similar in form to those for waveform configuration 1.

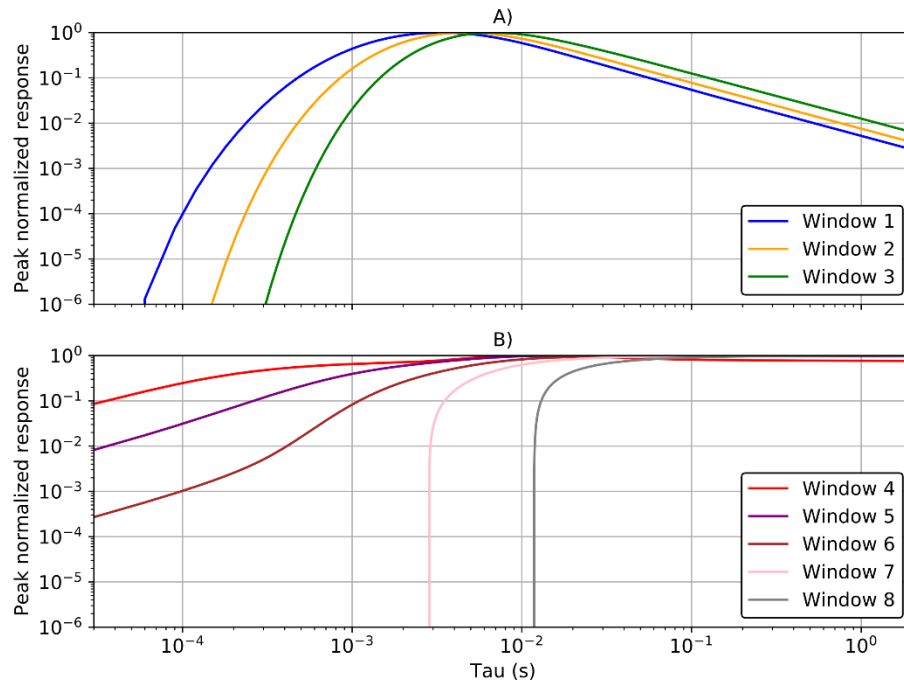


Figure 28: Peak normalized window response as a function of  $\tau$ , for the 30 Hz signal with the pulse and window width unreduced A) off-time B) on-time

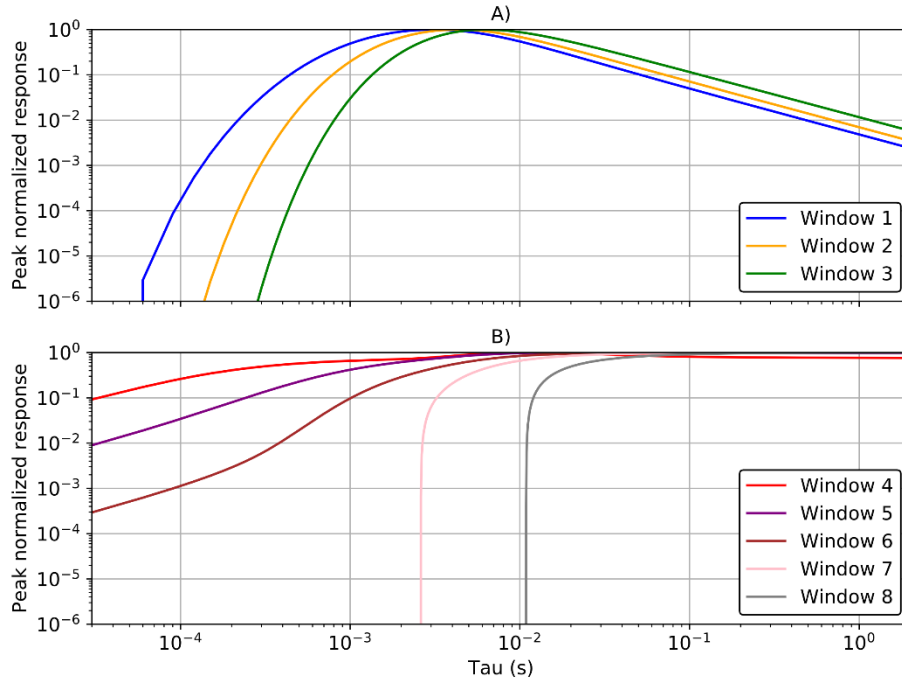


Figure 29: Peak normalized window response as a function of  $\tau$ , for the 32.5 Hz signal with the pulse and window width reduced by a factor of 32.5/30 A) off-time B) on-time

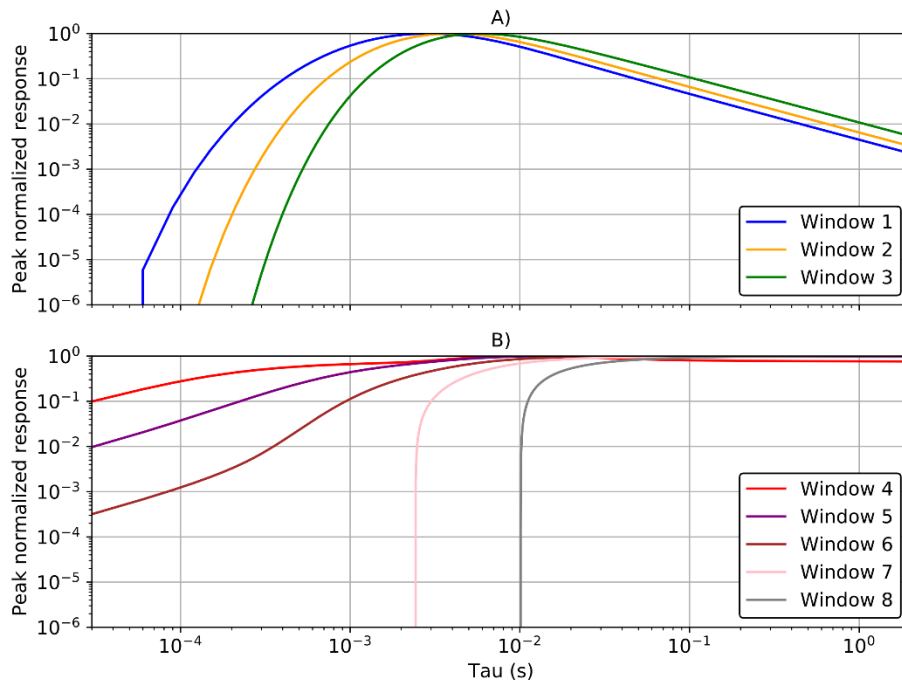


Figure 30: Peak normalized window response as a function of  $\tau$ , for the 35 Hz signal with the pulse and window width reduced by a factor of 35/30 A) off-time B) on-time